remote sensing

MDPI

Article

Bistatic and Stereoscopic Configurations for HF Radar

Stuart Anderson

Physics Department, University of Adelaide, Adelaide 5005, Australia; stuart.anderson@adelaide.edu.au

Received: 20 January 2020; Accepted: 18 February 2020; Published: 20 February 2020

Abstract: Most HF radars operate in a monostatic or quasi-monostatic configuration. The collocation of transmit and receive facilities simplifies testing and maintenance, reduces demands on communications networks, and enables the use of established and relatively straightforward signal processing and data interpretation techniques. Radars of this type are well-suited to missions such as current mapping, waveheight measurement, and the detection of ships and aircraft. The high scientific, defense, and economic value of the radar products is evident from the fact that hundreds of HF radars are presently in operation, the great majority of them relying on the surface wave mode of propagation, though some systems employ line-of-sight or skywave modalities. Yet, notwithstanding the versatility and proven capabilities of monostatic HF radars, there are some types of observations for which the monostatic geometry renders them less effective. In these cases, one must turn to more general radar configurations, including those that employ a multiplicity of propagation modalities to achieve the desired illumination, scattering selectivity, and echo reception. In this paper, we survey some of the considerations that arise with bistatic HF radar configurations, explore some of the missions for which they are optimal, and describe some practical techniques that can guide their design and deployment.

Keywords: HF radar; bistatic radar; HFSWR; OTH radar

1. Introduction

Remote sensing of our geophysical environment by means of radio waves in the HF band is now a truly global activity, with decametric radars operating in scores of countries, and on every continent [1]. In a number of instances, international collaborations facilitate the integration of the outputs from individual radars to yield regional or even basin-scale products, thereby increasing the quality, diversity, and utility of the derived information [2].

The overwhelming majority of these radars operate in the conventional monostatic configuration, with the transmitting and receiving systems collocated or closely spaced (the term quasi-monostatic is often used in this case). This simple geometry has obvious advantages in terms of cost, siting requirements, communications, maintenance, signal processing, and echo interpretation, and has been adopted by HF radars exploiting line-of-sight, surface wave, and skywave propagation modalities.

All these considerations notwithstanding, in some circumstances, there can be compelling reasons to implement bistatic configurations, often defined as geometries in which the separation between transmitter and receiver is comparable with the range to the zones being interrogated. Factors that can drive this decision include energy budget, desire to exploit hybrid propagation modes, scattering characteristics of the targets of interest, properties of the clutter, survivability, and covertness. Bistatic HF radars with very specific missions have been deployed since the 1960s, predominantly in defense applications, but the convenience of monostatic designs and the adequacy of their standard remote sensing products have tended to discourage wider adoption of bistatic configurations.

Once we allow for the separation of transmit and receive facilities, many possible configurations emerge. Each of these subsystems can be located on land, at sea, in the air, or even in space, with a

range of propagation mode combinations possible for the signal paths from transmitter to target and target to receiver. Of these, line-of-sight, ground wave (we shall use the term *surface wave* throughout this paper, though strictly it refers to only one component of the total field−the dominant one at over-the-horizon ranges), and skywave modes are by far the most common, though more exotic propagation mechanisms have been explored. Figure 1 presents a taxonomy of the main configurations; those that are understood to have been implemented, or at least reached the advanced design and experimentation phase [3], are indicated by the colored dots (E. Lyon, personal communication, May 19, 2015).

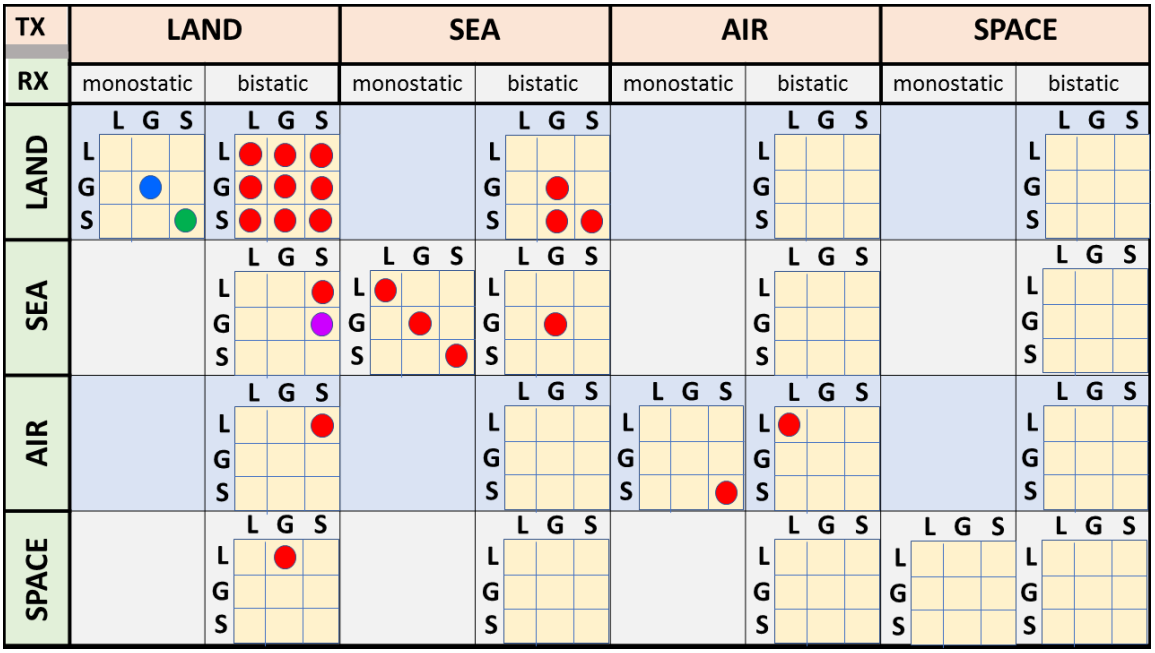

Figure 1. A taxonomy of HF radar configurations. The conventional monostatic surface wave and skywave radars are indicated with blue and green markers, respectively; the topical hybrid sky–surface wave configuration is shown by the magenta marker.

An obvious generalization of these single radar configurations is the deployment of multiple radars to interrogate a common area of interest. This is the standard modus operandi of current mapping HF surface wave radars (HFSWR) such as the CODAR SeaSonde [4] and the Helzel Messtechnik WERA [5], where two or more measurements of radial velocity are combined to yield a resultant vector. We note that measurements from these two distinct radar designs—based on direction-finding and beam-forming, respectively—can be combined to expand network coverage and reduce down-time [6]. Skywave radar networks with overlapping coverage have been operational in Australia (JORN) [7] and the United States (ROTHR) [8] for decades; not surprisingly, there are many issues to be taken into account when designing such configurations [9,10]. The term stereoscopic has been used to describe these multi-monostatic configurations; other applications include ship target dynamic signature analysis and excitation of nonlinear scattering mechanisms.

Another generalisation is the use of relay stations; that is, combined receive–transmit facilities that acquire the signal radiated by the primary radar transmitter, amplify it, possibly with additional modulation, and then reradiate it, thereby extending the range of the system or facilitating other radar functions.

This diverse array of system geometries offers many opportunities for remote sensing. In particular, the ability to extend the range of Bragg resonant scattering to lower wavenumbers opens the way to observing some environmental phenomena to which monostatic radars are insensitive. One example of this is the determination of sea ice parameters. Short sea waves are rapidly attenuated as they enter

the marginal ice zone; only long waves penetrate to useful distances into the ice field. The sea ice properties are encoded in the radar Doppler spectrum, most visibly in the first-order peaks [11]. For a monostatic radar to observe these peaks, it would need to operate at a very low frequency, below those employed by present-day HF radars, but a bistatic geometry enables the returns from longer waves to be measured. Another example is the investigation of the physics of the ionosphere via analysis of impressed phase modulation [12,13], wavefront distortion [14], and polarization transformation [15] of oblique (bistatic) radar reflections; these are largely inaccessible to monostatic radars.

In this paper, we explore many of the issues that arise with bistatic HF radar configurations, basing our analysis on the formal radar process model presented in the following section. After examining the implications for the component elements of the radar observation process, we proceed to describe some specific radar missions that benefit from the physics of bistatic scattering and/or hybrid propagation modes. The term hybrid is often applied to configurations where the outbound and inbound propagation modalities are different; that is, they lie off the diagonals in the boxes of Figure 1. Along the way, we describe and illustrate some practical techniques that can serve as a guide to bistatic HF radar design and deployment. In particular, we look at the problem of site selection, a challenge that is compounded by the need to address multiple radar missions.

2. The General Radar Process Model

The radar process model formulation first introduced in [16] is ideally suited for our purpose as it makes explicit the temporal sequence of the signal trajectory and of this in mind, and noting that multizone scattering in the course of signal propagation (see below) has been observed to be significant for both skywave and surface wave HF radars [17,18], the formulation of the radar process is expressed as a concatenation of operators,

$$s = \sum_{n_B=1}^{N} \widetilde{R}\left[\prod_{j=1}^{n_B} \widetilde{M}_{S(j)}^{S\lfloor j+1\rfloor}\widetilde{S}(j)\right]\widetilde{M}_{T}^{S(1)}\widetilde{T}w + \sum_{l=1}^{N_J}\sum_{m_B=1}^{M} \widetilde{R}\left[\prod_{k=1}^{n_B} \widetilde{M}_{S(k)}^{S\lfloor k+1\rfloor}\widetilde{S}(k)\right]\widetilde{M}_{N}^{S(1)}n_l + m \tag{1}$$

where

w represents the selected waveform,
$\widetilde{T}$ represents the transmitting complex, including amplifiers and antennas,
$\widetilde{M}_{T}^{S(1)}$ represents propagation from transmitter to the first scattering zone,
$\widetilde{S}(j)$ represents all scattering processes in the j-th scattering zone,
$\widetilde{M}_{S(j)}^{S\lfloor j+1\rfloor}$ represents propagation from the j-th scattering zone to the (j+1)-th zone,
n_B denotes the number of scattering zones that the signal visits on a specific route from the transmitter to the receiver,
N_J denotes the number of external noise sources or jammers,
$\widetilde{M}_{N}^{S(1)}$ represents propagation from the i-th noise source to its first scattering zone,
m_B denotes the number of scattering zones that the i-th noise emission visits on a specific route from its source to the receiver,
N, M denote the maximum number of zones visited by signal and external noise, respectively,
$\widetilde{R}$ represents the receiving complex, including antennas and receivers,
m represents internal noise,
s represents the signal delivered to the processing stage.

If the transmitter and/or receiver are in motion, as with shipborne radars, for example, a slight generalization is in order. Adopting the frame-hopping paradigm, we insert Lorenz transformation operators:

$$\widetilde{T} \rightarrow \widetilde{L}_T\widetilde{T} \tag{2}$$

and

$$\widetilde{R} \rightarrow \widetilde{R}\,\widetilde{L}_R \tag{3}$$

to take kinematic effects into account.

The effective design of bistatic HF radar systems requires decisions that involve all the terms in the process model, singly, pairwise, or collectively. Ultimately, the design problem is one of optimization; that is, finding the best combination of siting and radar parameters as measured by performance over the set of missions to be addressed. In general, this is a multi-objective problem as radars may be designed to perform air and surface surveillance as well as remote sensing of one or more geophysical variables. Later in this paper, we will describe tools for achieving this optimization, but first we examine some of the most important considerations associated with the individual operators.

3. Consequences of Bistatic Geometry on the Radar Process Model Operators

3.1. Waveform

Most HF radars nowadays employ a variant of the linear FMCW waveform, ranging from a continuous signal, through interrupted FMCW, to FM pulses with a low duty cycle. Interrupted versions include notched sweeps as well as frequency-hopping and spaced sweep formats. In addition to the FMCW class, phase-coded pulse waveforms can still be heard. For most of these options, MIMO (multiple input, multiple output) implementations are possible.

When one moves from monostatic or quasi-monostatic to the bistatic case, several considerations need to be kept in mind. First, the separation of transmit and receive facilities greatly reduces the problem of self-interference, thereby expanding the waveform parameter space. For the moment, we set aside the case where radars in a stereoscopic configuration are sharing a common transmission frequency band. Second, it is well known that range-folded echoes pose a serious hazard for monostatic radars, arising from the combination of long-range propagation of HF radiowaves and the abundance of ionospheric and terrestrial scatterers. As illustrated in Figure 2, bistatic configurations offer a greater freedom with choice of waveform repetition frequency because the range-ambiguous zones of illumination are displaced from those of the receiving system. We note here that the use of non-repetitive waveforms is another tool for reducing this threat, though few HF radars presently employ such signals.

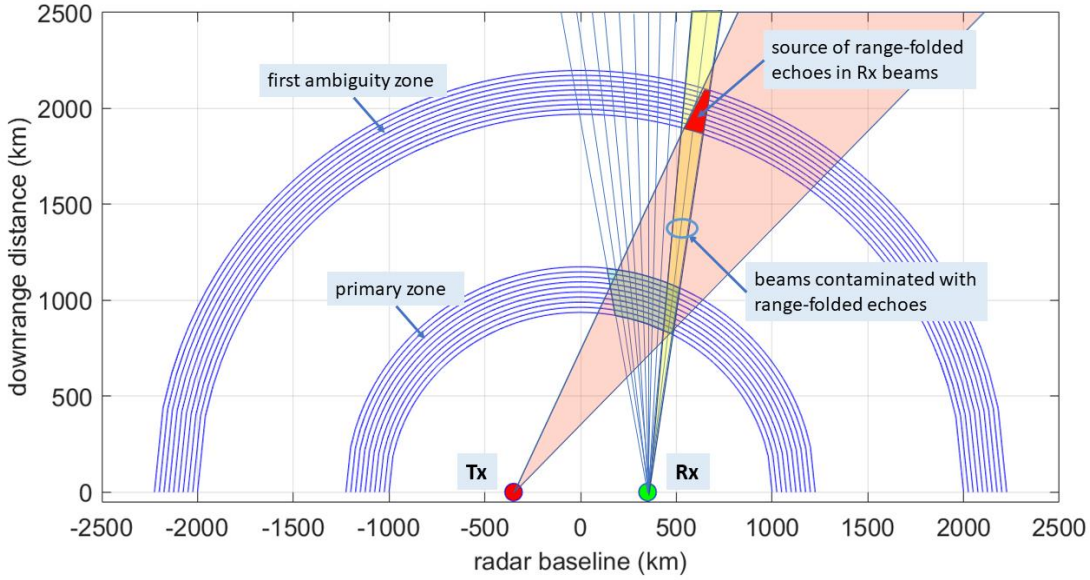

Figure 2. The problem of range-ambiguous echoes associated with periodic waveforms is greatly reduced with bistatic configurations. These enable one to steer the receiver beams over the desired ambiguity zone whilst rejecting unwanted returns.

Yet, even bistatic systems are advised to take account of the far-range illumination pattern as the magnitude of unwanted environmental echoes may be sufficient to disrupt through receiving array

sidelobes. Third, an associated problem is the prospect of round-the-world (RTW) propagation—in powerful HF skywave radars, signals have been observed after three transits around the Earth. Of course, for low-power radars, background noise will almost invariably swamp RTW returns. Fourth, when pulsed waveforms are used, the fact that bistatic geometry couples time delay to angle-of-arrival may require that one implements a pulse-chasing capability [19], with its attendant penalties. Fifth, the spatial properties of bistatic resolution cells are well-known [20], but less attention has been paid to what we might call the Doppler sensitivity, $\frac{\partial \omega}{\partial v}$, where ω is the Doppler shift and v is the target speed. To quantify this, recall that the bistatic Doppler shift of a target with velocity $\vec{v}$ at location x given by

$$\omega = -\frac{2\pi}{\lambda}\frac{d}{dt}\left(r_T^x + r_x^R\right) = -k\left(\hat{r}_T^x \cdot \vec{v} + \vec{r}_x^R \cdot \vec{v}\right) = -k\left(\hat{r}_T^x + \hat{r}_x^R\right)\cdot \vec{v} = -2k\, cos\left(\frac{\varphi}{2}\right) v.\cos\beta \tag{4}$$

with φ the bistatic angle and β the target heading relative to the bisector axis; hence,

$$\frac{\partial \omega}{\partial v} = -2k\, cos\left(\frac{\varphi}{2}\right).v\, cos\, \beta \tag{5}$$

The Doppler sensitivity loss factor $\cos\left(\frac{\varphi}{2}\right)$ is one component of the price we pay in return for whatever advantages we can extract from employing a bistatic configuration.

3.2. Transmitting Facility

Central to the design of the transmitting facility is the orientation of the illumination pattern relative to that of the receiver. For any given location $\vec{r}$ in the common zone, the radiated signal amplitude is proportional to $\widetilde{M}_T^{\vec{r}}\, \widetilde{T}(\theta, \varphi)w$, or simply $\widetilde{M}_T^{\vec{r}}\, \widetilde{T}(\varphi)w$ for HFSWR. The radar designer has the option to orient the maximum directive gain of the transmitting array towards that region in the receiving facility's field of view, which has been accorded the highest priority. More generally, for signal-to-noise dominated missions, we can formulate the HFSWR orientation problem as one of maximizing the figure of merit (FOM) of the priority-weighted pattern,

$$FOM = max_{\varphi_0} \iint_R P\left(\vec{r}\right) \widetilde{M}_{\vec{r}}^R \widetilde{M}_T^{\vec{r}}\, \widetilde{T}(\varphi, \varphi_0)w\, d\vec{r} \tag{6}$$

where φ_0 is the nominal boresight orientation of the transmit array and $P\left(\vec{r}\right)$ represents the priority weighting over the receiver processing zone R.

A complication that arises with clutter-related missions of HFSWR is the phenomenon of multiple scattering [21,22]. This can corrupt the received echoes when the sea state is significant, so in addition to providing sufficient incident power density, a sophisticated transmit antenna design would attempt to minimize the associated contributions, relative to the echoes received via the primary propagation path. To do this requires a regional wave climatology but is otherwise straightforward.

3.3. Propagation

The involvement of distinct outbound and inbound propagation paths has major ramifications for HF skywave radar, with a lesser, though still observable, impact on HFSWR. For monostatic skywave radars, frequency management systems probe the ionosphere and determine (i) the frequency band providing adequate power density in the target zone, and (ii) some measure of the quality of the propagation channel [23]. With bistatic configurations, the frequency that works best for propagation from transmitter to target zone will often be poor for propagation from target zone to receiver; in this case, the optimum frequency will effect a compromise, and may, on occasion, take a highly non-intuitive value.

In order to quantify the impact on performance, we can exploit the geometrical congruence of a single bistatic signal path and two monostatic paths [24]. Figure 3 shows the concept underlying this technique.

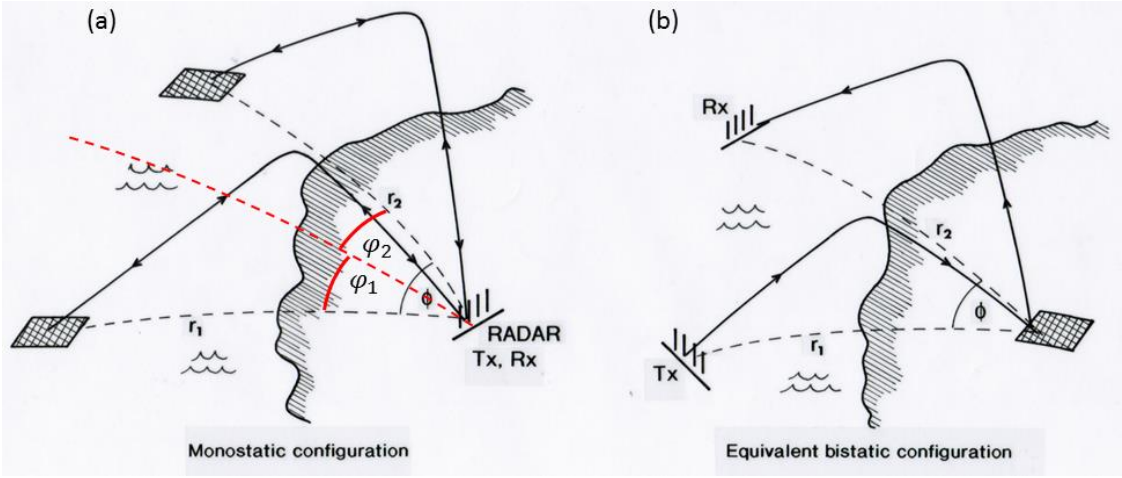

Figure 3. The geometrical congruence of (**a**) a pair of monostatic radar observations, and (**b**) a single bistatic radar observation. To see the equivalence, simply imagine that the area shown as land is actually sea and the area shown as sea is actually land, whereby Figure 3b appears as a land-based bistatic radar.

The first emission travels from the monostatic radar at location X to the target zone at relative coordinates (r_1, φ_1), scatters, and returns to the radar. Using a scalar form of (1) for notational simplicity, the complex amplitude of the received signal is given by

$$s_1 = R(\varphi_1) M^{X}_{\vec{r}_1} S\left(\vec{r}_1\right) M^{\vec{r}_1}_{X} T(\varphi_1) w \tag{7}$$

so the received power is $|s_1|^2$. Now, write $M^{\vec{r}_1}_{X} = a_1^T e^{i\psi_1^T}$ and $M^{X}_{\vec{r}_1} = a_1^R e^{i\psi_1^R}$. We can identify a_1^T as the one-way propagation amplitude loss factor for the outbound signal and a_1^R as the corresponding amplitude loss factor for the inbound signal. Power loss factors are then simply $\left|a_1^T\right|^2$ and $\left|a_1^R\right|^2$, and the propagation power loss for the two-way process is $\left|a_1^T\right|^2 . \left|a_1^R\right|^2$.

A second observation is then made in a different direction, to a target zone at coordinates (r_2, φ_2),

$$s_2 = R(\varphi_2) M^{X}_{\vec{r}_2} S\left(\vec{r}_2\right) M^{\vec{r}_2}_{X} T(\varphi_2) w \tag{8}$$

with two-way propagation loss $\left|a_2^T\right|^2 . \left|a_2^R\right|^2$, as shown in Figure 3a. Now imagine that there is a transmitter at location (r_1, φ_1) and a receiver at (r_2, φ_2) as shown in Figure 3b; that is, a bistatic radar configuration interrogating the region previously occupied by the monostatic radar. The complex amplitude for this case is given by

$$s_3 = R(\varphi_2) M^{\vec{r}_2}_{X} S(X) M^{X}_{\vec{r}_1} T(\varphi_1) w \tag{9}$$

where we have taken the orientation of the imagined arrays to be parallel to those of the monostatic system. Now, the propagation paths satisfy reciprocity, $M^{X}_{\vec{r}_1} = M^{\vec{r}_1}_{X}$ and $M^{\vec{r}_2}_{X} = M^{X}_{\vec{r}_2}$. Further, the gain patterns of the transmit and receive arrays are strongly determined by the array apertures but vary only weakly with steer angle over moderate departures from boresight. Thus, we can write

$T(\varphi_2) = \alpha\, T(\varphi_1)$ and $R(\varphi_2) = \beta R(\varphi_1)$ where $0.87 < \alpha, \beta < 1$ for a radar whose arrays each steer over a 60° arc. Substituting in (9), and invoking (7) and (8),

$$\begin{aligned} s_3 = R(\varphi_2)M_X^{\vec{r}_2}S(X)M_{\vec{r}_1}^X T(\varphi_1)w = \sqrt{s_3^2} \\ = \sqrt{R(\varphi_2)M_X^{\vec{r}_2}S(X)M_{\vec{r}_1}^X T(\varphi_1)w.R(\varphi_2)M_X^{\vec{r}_2}S(X)M_{\vec{r}_1}^X T(\varphi_1)w} \\ = S(X)\sqrt{R(\varphi_2)M_{\vec{r}_2}^X M_{\vec{r}_1}^X \tfrac{T(\varphi_2)}{\alpha}w.R(\varphi_1)M_X^{\vec{r}_2}M_X^{\vec{r}_1}T(\varphi_1)w} \\ = S(X)\sqrt{R(\varphi_2)M_{\vec{r}_2}^X M_X^{\vec{r}_2}\tfrac{T(\varphi_2)}{\alpha}w.\beta R(\varphi_1)M_{\vec{r}_1}^X M_X^{\vec{r}_1}T(\varphi_1)w} \\ = \frac{S(X)}{\sqrt{S(\vec{r}_1)S(\vec{r}_2)}}\cdot\sqrt{\tfrac{\beta}{\alpha}R(\varphi_1)M_{\vec{r}_1}^X S(\vec{r}_1)M_X^{\vec{r}_1}T(\varphi_1)w.R(\varphi_2)M_{\vec{r}_2}^X S(\vec{r}_2)M_X^{\vec{r}_2}T(\varphi_2)w} \\ = \frac{S(X)}{\sqrt{S(\vec{r}_1)S(\vec{r}_2)}}\sqrt{\tfrac{\beta}{\alpha}}\cdot\sqrt{s_1 s_2} \approx \frac{S(X)}{\sqrt{S(\vec{r}_1)S(\vec{r}_2)}}\cdot\sqrt{s_1 s_2} \end{aligned} \quad (10)$$

The magnitudes of $S(\vec{r}_1)$ and $S(\vec{r}_2)$ can be estimated by inversion of the respective Doppler spectra, or even approximated at zero cost by assuming fully developed seas—typically valid for HF frequencies above 15 MHz. The steer directivity loss factor $\sqrt{\frac{\beta}{\alpha}} \approx 1$ so its effect is insignificant compared with the variability of the other terms. Thus, from measurements of the returned clutter power from monostatic observations s_1 and s_2, we can predict the echo power for the bistatic configuration observation s_3 for an arbitrary specified scattering coefficient $S(X)$. One point to note here is that we have simplified the discussion by ignoring the polarization domain; this is not a significant issue for HFSWR and can be avoided in the skywave radar case by a combination of spatial and temporal averaging.

HF skywave radars routinely collect backscatter ionograms (BSI) over the arc of coverage, typically out to a range of 5000–6000 km, so there is a wealth of propagation data available from which to derive statistical predictions that can be used for bistatic system design. A representative BSI is shown in Figure 4, with the instantaneous range depth marked for a nominal radar frequency of 15 MHz. Assuming a slow variation with azimuth, both r_1 and r_2 need to lie between 1400 km and 2300 km. Figure 5 shows an instance of an inferred sub-clutter visibility (SCV) map computed for a representative radar network (the monostatic input data are real but not obtained from these radars).

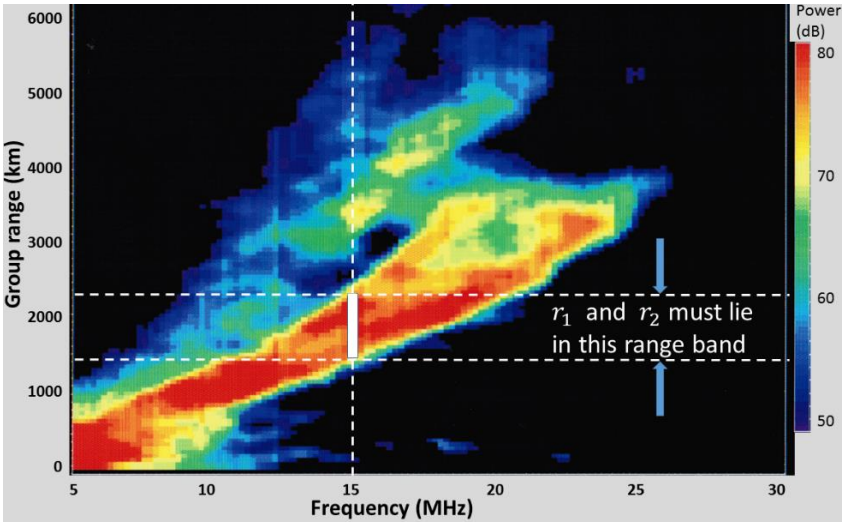

Figure 4. A backscatter ionogram—a map of echo strength as a function of (group) range and radar frequency. The dashed lines show, for a representative frequency, how the outbound and inbound group ranges must both lie in the band indicated for the system to operate successfully.

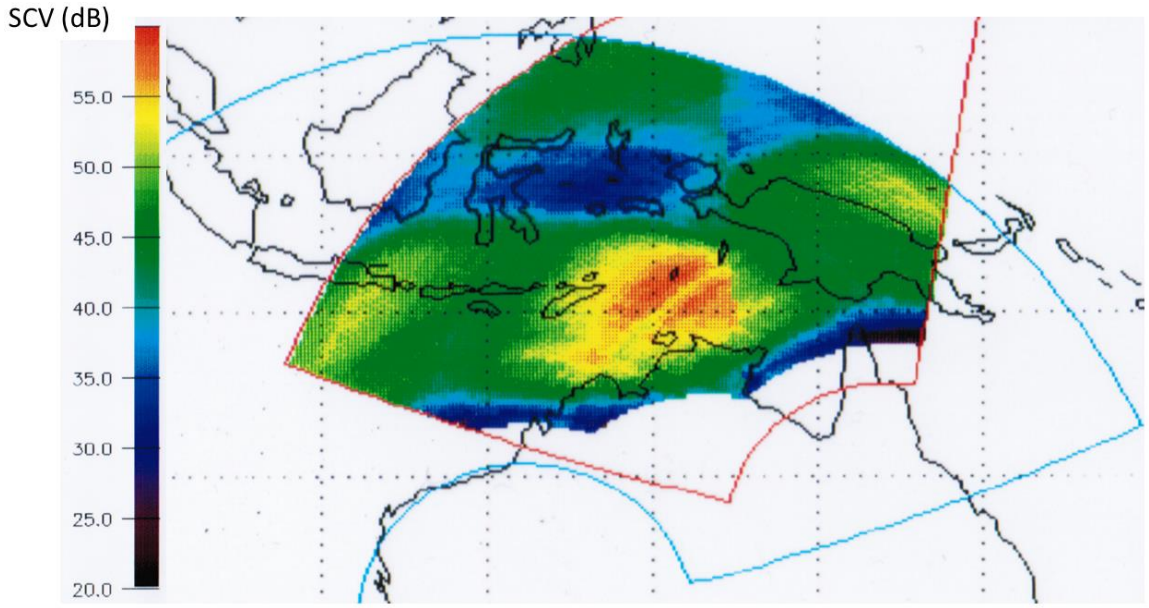

Figure 5. A map showing a single instance of the predicted bistatic sub-clutter visibility (clutter-to-noise ratio) in the overlap region of two skywave radars, as inferred using the geometrical congruence technique from a single azimuthal scan recorded with a separate monostatic radar.

While it is necessary to exceed some target-specific threshold of power density in order to achieve detection, for slow-moving targets, such as ships, that may not be sufficient. The presence of multimode propagation and phase path fluctuations associated with field line resonances and other ionospheric disturbances can blur the Doppler spectrum of the radar returns and thereby obscure the desired echoes. This raises the question: Can we extend the analysis discussed in the preceding paragraphs so as to obtain statistical information on the phase path modulation spectrum over bistatic paths?

The answer is a qualified 'yes'. Techniques to estimate and then correct for phase path variations have been developed and installed in operational systems since the 1980s [12,13] so the individual phase path modulation time series are available for each leg of the synthesized bistatic path. A rudimentary synthesis approach would simply concatenate the phase modulation histories, then halve them, but that could introduce Doppler spreading due to phase discontinuity at the junction point. A superior method involves first phase-shifting the second half to ensure phase continuity and then applying a conjugate taper weighting around the junction to affect a smooth first derivative.

This approach works for the most important class of fluctuations, where the spatial scale is of the order of 10^2 km, and latitude-dependent, being linked to the geomagnetic field line resonances (FLR) that are observed as micro-pulsations at ground level. At times, other dynamical processes cause fluctuations over much smaller spatial scales. Figure 6 illustrates these two types of modulation: Each frame shows the measured phase fluctuation time series over a two-way skywave channel. In Figure 6a, the modulation estimated from the echoes originating in four individual range cells spaced over a range depth of about 150 km shows a high degree of spatial correlation, suggesting that the outbound and inbound legs of a bistatic skywave radar observation would experience related modulation sequences. In contrast, when other types of modulation prevail, the paths can experience uncorrelated and often more erratic modulations. In Figure 6b, the cells shown are spaced over a total of only 20 km, yet the modulation patterns are quite distinct. In both cases, we can construct a simulated bistatic path resultant modulation sequence, using the ideas of the previous paragraph, but only for the former type can we hope to associate the observed modulation with the known properties of geophysical wave processes in the ionosphere.

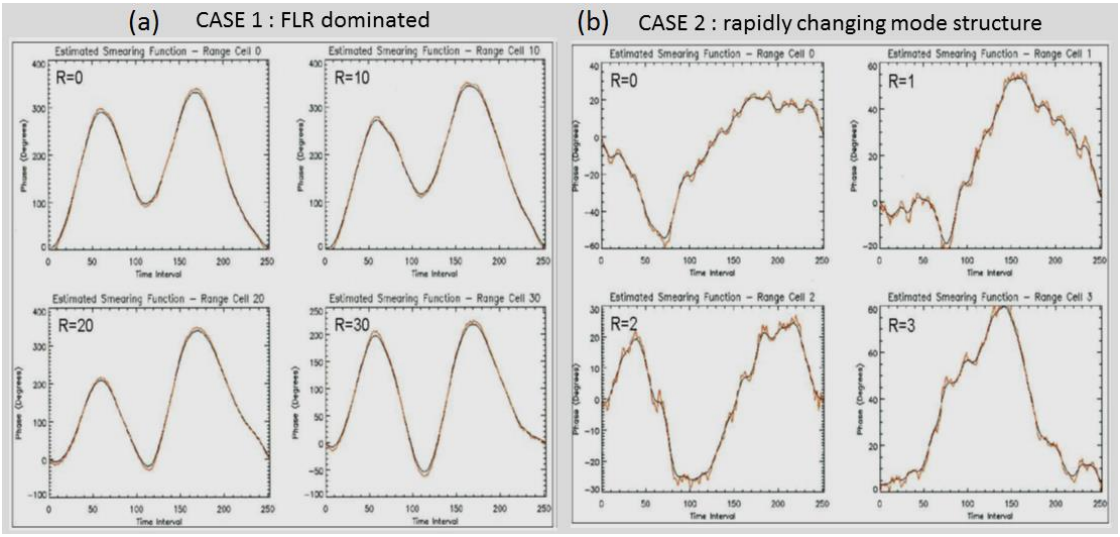

Figure 6. Phase modulation sequences measured over skywave propagation paths; (**a**) an example of a field line resonance modulation, with slow spatial variation over a distance of 150 km, and (**b**) an example where the modulation arises from other geophysical mechanisms, with spatial decorrelation occurring within 20 km.

It is perhaps apposite to note here that an operationally significant relative of the problem of joint path optimization is the converse—the selection of frequencies that guarantee strong propagation over one path and little over the other for the same radar frequency. Such a bistatic configuration has direct relevance to the detection of nonlinear target echoes and the ability to suppress sea clutter by many tens of dB. A description of this scheme can be found in [25].

3.4. Scattering

The ability of HF radar to address a wide range of missions brings with it the need for mathematical techniques for computing the radar signatures of the diverse phenomena involved. Bistatic HF radar has been implemented in the form of operational systems since the 1960s but, for most of its history, practice has dominated theory. We can perceive four main lines of development in HF scattering theory: One for the ocean surface, one for plasma formations in the ionosphere, one for land surfaces, and one for discrete targets such as ships, aircraft, and missiles.

3.4.1. Scattering from the Ocean Surface

The perturbation theoretic approach of Barrick [26], building on the Rice theory for scattering from static rough surfaces [27], has served as the cornerstone of HF radar oceanography for the past five decades. Quite a few generalizations of the Barrick theory have appeared over the years (e.g., [28–30]), as well as a different approach [31] based on the Walsh theory for scattering from static surfaces [32] and extended by Gill and co-workers (e.g., [33–36]). As ocean applications of HF radars dominate, and as bistatic configurations become more widespread, it is hardly surprising to find an emerging literature of papers that apply the fundamental theories to particular circumstances. As a guide, we have tabulated some of these bistatic scatter papers against key parameters: (i) The perturbation order of the approximation, (ii) the scattering geometry, (iii) whether platform motions were taken into account, (iv) the polarization states addressed, and (v) the hydrodynamic dispersion relation employed. This file is available from the author.

The general expression for the scattered field in $\left(\vec{k},\omega\right)$ space, to second order, has the form

$$\begin{aligned} S\left(\vec{k},\omega\right) &= \int d\vec{k}_{scat}\widetilde{R}\left(\vec{k}_{inc}\right)\delta\left(\vec{k}_{scat}-\vec{k}_{inc}+2\vec{k}_{inc}\cdot\hat{n}\,\hat{n}\right)\delta(\omega-\omega_0) \\ &+\int d\vec{\kappa}_1\,F_1\left(\vec{k}_{scat},\vec{k}_{inc},\vec{\kappa}_1\right)\delta\left(\vec{k}_{scat}-\vec{k}_{inc}+\vec{\kappa}_1\right)\delta\left(\omega-\omega_0+\Omega\left(\vec{\kappa}_1\right)\right) \\ +\int\int d\vec{\kappa}_1\,d\vec{\kappa}_2\,F_2&\left(\vec{k}_{scat},\vec{k}_{inc},\vec{\kappa}_1,\vec{\kappa}_2\right)\delta\left(\vec{k}_{scat}-\vec{k}_{inc}+\vec{\kappa}_1+\vec{\kappa}_2\right)\times\delta\left(\omega-\omega_0+\Omega\left(\vec{\kappa}_2\right)+\Omega\left(\vec{\kappa}_1\right)\right) \end{aligned} \tag{11}$$

In this equation, the dispersion relation appears as $\Omega\left(\vec{\kappa}_i\right)$; it is this function that determines the contours of integration that yield the Doppler power spectral density. Recent investigations of HF scatter from sea ice motivated the development of a computational model able to solve for any explicit dispersion relation [11,37]. Expressions for the kernel functions F_1 and F_2 can be found in the cited literature, while the Fresnel reflection coefficient $\widetilde{R}$ is a function of the water temperature and salinity.

Viewed diagrammatically in the spatial frequency domain, as shown in Figure 7, an important feature of bistatic Bragg scattering becomes evident, namely the smaller modulus of the resultant wave vector increment, shown in black. At first order, this means that longer ocean waves can be measured directly, while at second order, it means that a broad angular spread of the shorter waves in the participating wave field favors the scattering contributions.

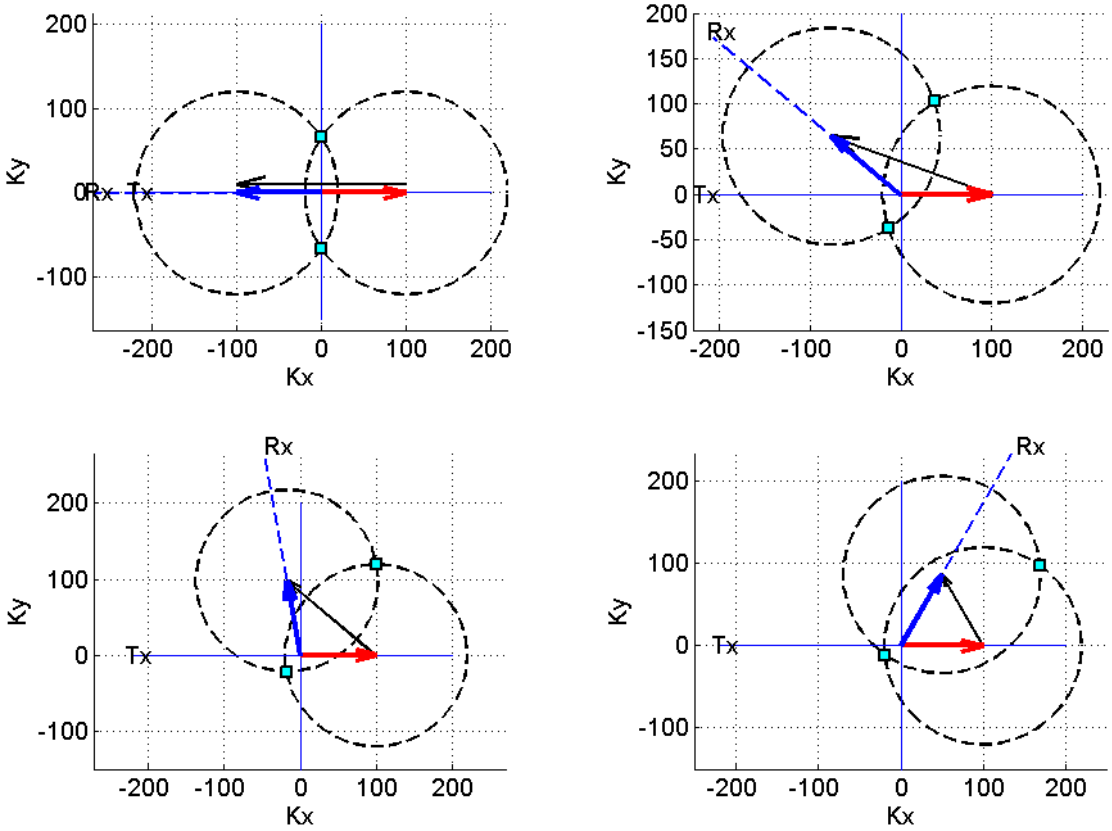

Figure 7. Double Bragg scattering processes in $\vec{\kappa}$-space. The red vector represents the incident radiowave, the blue vector the scattered radiowave, and the black vector, the required change in wave vector to be delivered by pairs of ocean waves whose $\vec{\kappa}$ -vectors meet at the intersection of the circles of given wavenumbers. Here they are drawn for the case of equal wavenumbers. Tx and Rx indicate the directions of the transmitter and receiver.

It is instructive to see the form of the Doppler spectrum as a function of the bistatic geometry for particular situations and as a function of various parameters. First, we present Figure 8, taken

from [18], which shows, at a most basic level, how a particular seastate modulates the frequency of the scattered signal depending on the scattering geometry: Back scatter, forward scatter, side scatter, or up scatter. In this example, only the VV (vertical in, vertical out) element of the polarization power scattering matrix is presented.

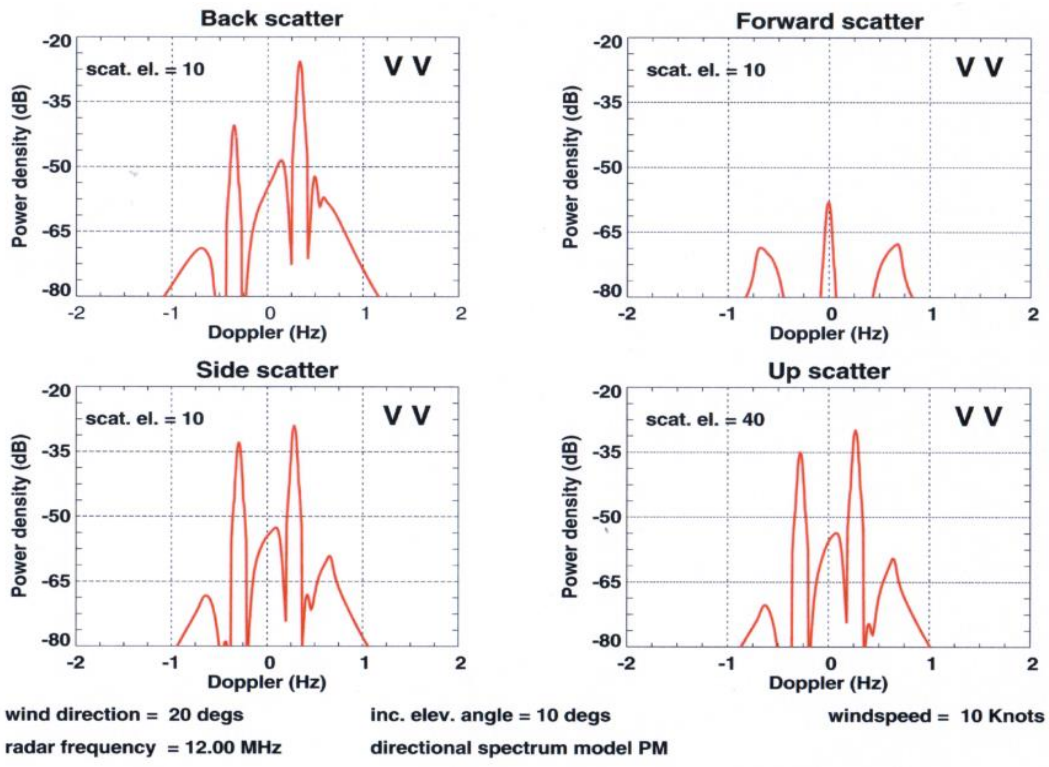

Figure 8. An example of the variation of the Doppler spectrum for representative bistatic scattering geometries incident on the same sea state: Backscatter, forward scatter, side scatter, and up scatter, as applicable to different HF radar configurations (reproduced from [18]).

Next, in Figures 9–11, we show the full polarization power scattering matrix for three different radar frequencies, in each case plotting the spectrum for four different bistatic skywave scattering geometries, at a fixed sea state. Here, 180° corresponds to backscatter, i.e., monostatic geometry. The vertical angles of incidence and reflection are 40° in all cases.

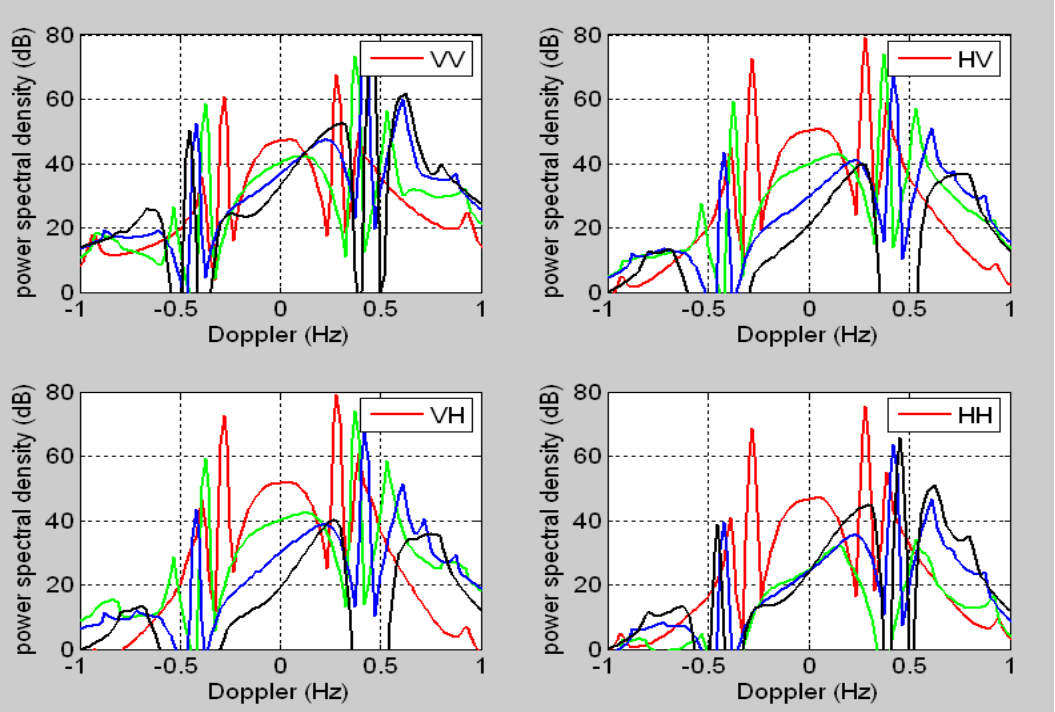

Figure 9. Sea clutter Doppler spectrum: φ = 45°(red), 90°(green), 135°(blue), 180°(black); F = 25 MHz.

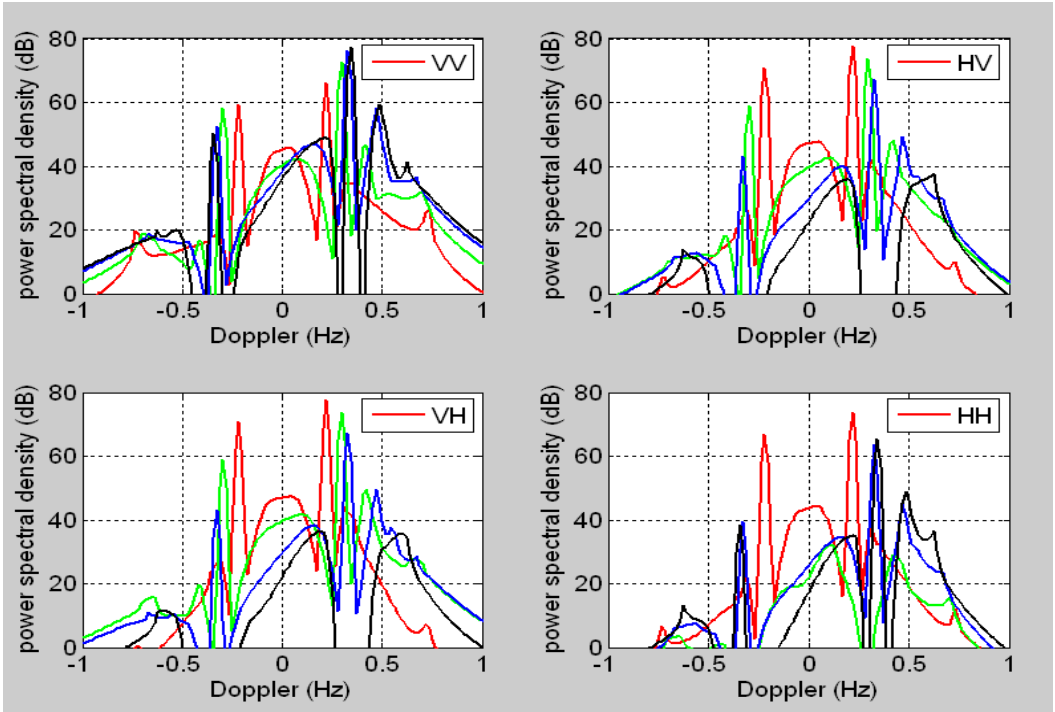

Figure 10. Sea clutter Doppler spectrum: φ = 45°(red), 90°(green), 135°(blue), 180°(black); F = 15 MHz.

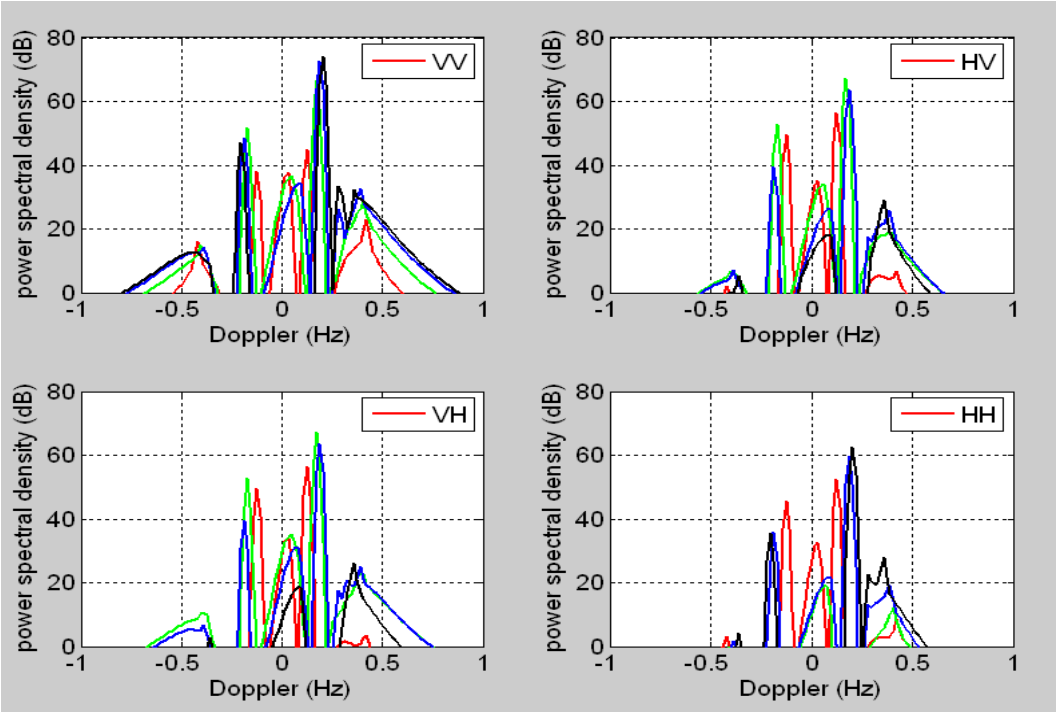

Figure 11. Sea clutter Doppler spectrum: φ = 45°(red), 90°(green), 135°(blue), 180°(black); F = 5 MHz.

Finally, in Figure 12, we present a range-Doppler map measured with a bistatic HFSWR, along with two modelled range-Doppler maps computed for scattering geometries close to that used for the measurement.

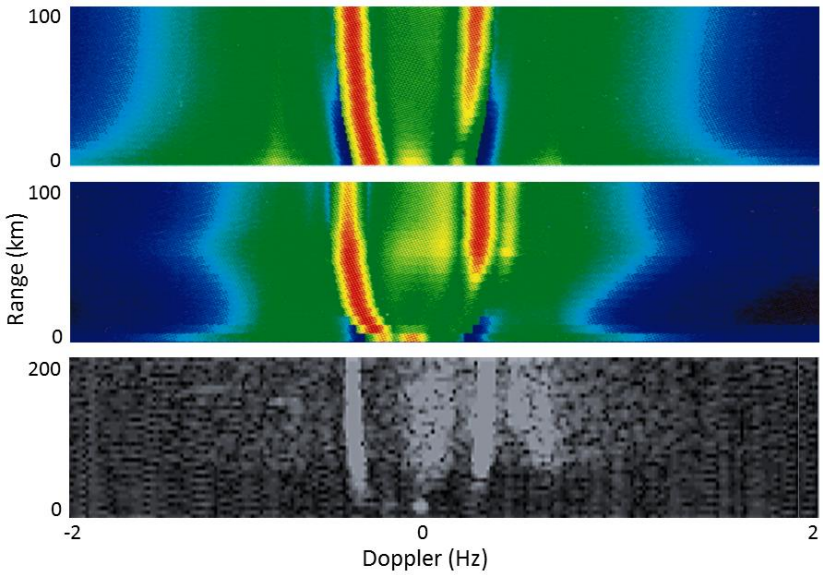

Figure 12. Modelled and measured Doppler spectra presented as range-Doppler maps. The variation of Bragg frequency with bistatic angle is clearly seen, especially at low ranges as the bistatic angle approaches its maximum. At near ranges, a decrease in signal power is evident in the measurement—this is due to the transmit antenna gain pattern falling off at angles close to the bearing to the receiver.

3.4.2. Scattering from Ships and Aircraft

Although target detection was once the province of HF radars deployed only for national defense, many low-power remote-sensing radars are now addressing this mission, primarily focusing on ship detection. Modelling HF radiowave scattering from ships and aircraft has been carried out for many decades by means of computational electromagnetic codes. Early work was almost exclusively carried out using the method-of-moments code NEC, but nowadays, other software packages such as FEKO, CST Studio, and HFSS are widely used, along with more advanced in-house codes. Here, we illustrate the general characteristics of bistatic HF radar cross sections (RCS) of ships and aircraft with results computed for the Fremantle-Class patrol boat 42 m in length, and the Aermacchi MB 326H aircraft, wingspan 10.6 m. These platforms are pictured in Figure 13.

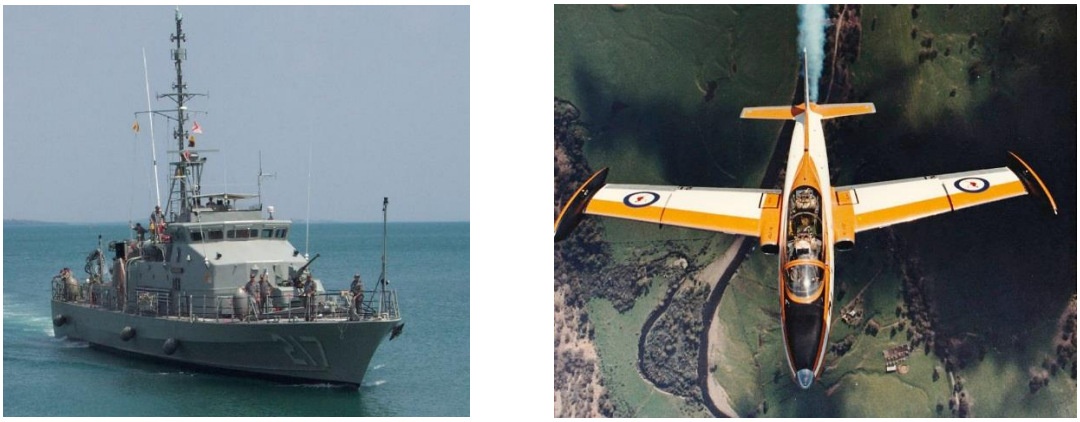

Figure 13. The Fremantle Class patrol boat and the Aermacchi MB 326H trainer aircraft.

A format developed to present bistatic HF radar cross section is shown in Figure 14. The figure shows the predicted bistatic RCS of the Fremantle Class patrol boat, evaluated at four different radar frequencies. More precisely, it shows the squared magnitude of the VV component of the polarization scattering matrix, but we will use the term RCS where no confusion is likely. This format uses columns to index the azimuthal angle at which the radar signal is incident on the target and rows to index the azimuthal angle of departure or scattered angle. In this example, the elevation angle is set to 0° (vertical angle of incidence=90°), which closely approximates the field structure for HFSWR. Below each panel showing the bistatic RCS is the monostatic RCS, i.e., the trailing diagonal of the matrix.

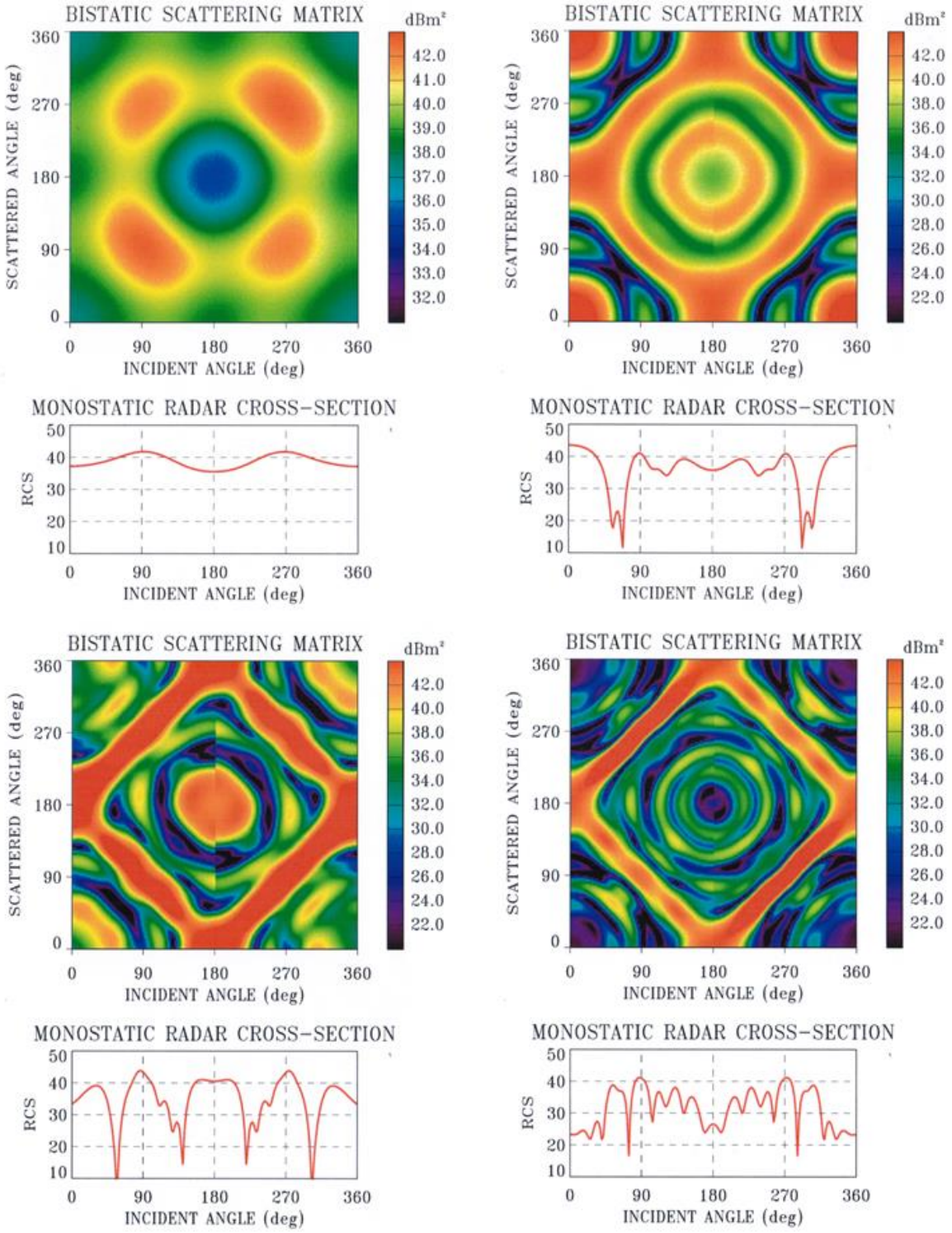

Figure 14. The bistatic RCS of the Fremantle Class patrol boat, evaluated at HF radar frequencies 5, 10, 15, and 20 MHz for HFSWR configurations. The lower panel in each case shows the monostatic RCS which is just the cut along the trailing diagonal.

For detection, we require that a ship echo exceed the clutter and noise power in the same Doppler bin by some margin ε; that is, there exists $\omega \in [-\Omega, \Omega]$ such that

$$s(\omega) > c(\omega) + n(\omega) + \varepsilon \tag{12}$$

where $s(\omega)$, $c(\omega)$, and $n(\omega)$ are the target, clutter, and noise power spectral densities. This situation is illustrated in Figure 15, where a nominal target echo is superimposed on Doppler spectra evaluated for four different sea states.

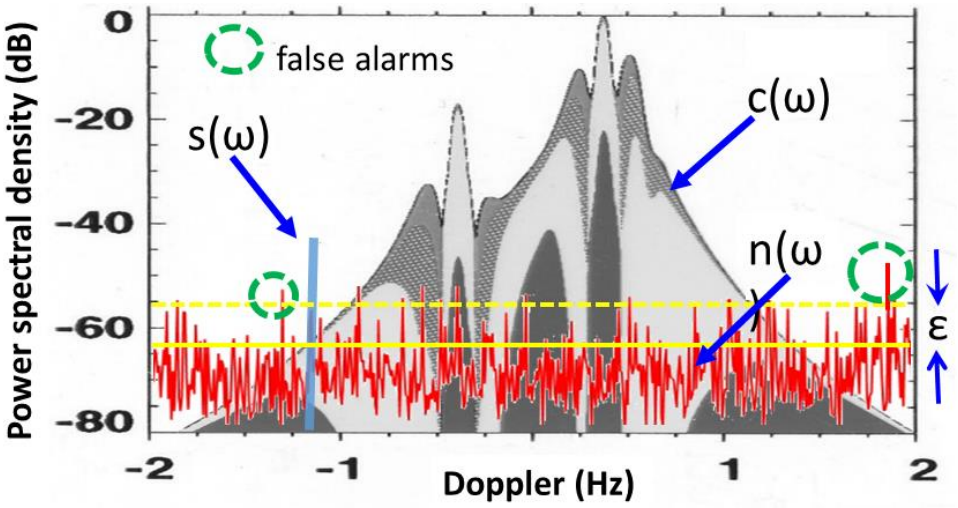

Figure 15. Ship detection in clutter and noise, showing the importance of thresholding.

The rich structure of the RCS patterns reveals the potential for exploitation by both the radar designer selecting sites for his transmit and receive systems, and the vessel seeking to minimize its detectability, in concert with other strategies that a clandestine mission might exploit. As we have seen in the previous section, the option of utilizing a bistatic configuration gives us an extra degree of freedom for 'controlling' the clutter spectrum.

While aircraft detection has seldom been a priority for HFSWR, it is certainly an established capability. Figure 16 uses a different format to show the VV RCS of the Aermacchi MB 326H as a function of azimuth (i.e., aspect) and radar frequency. The five panels correspond to different bistatic angles, namely, 0° (i.e., monostatic), 20°, 40°, 60°, and 80°. As aircraft move at speeds that carry them rapidly across typical HFSWR coverage, presenting a changing aspect, a distinctive temporal variation of echo strength can be observed, potentially useful for target classification.

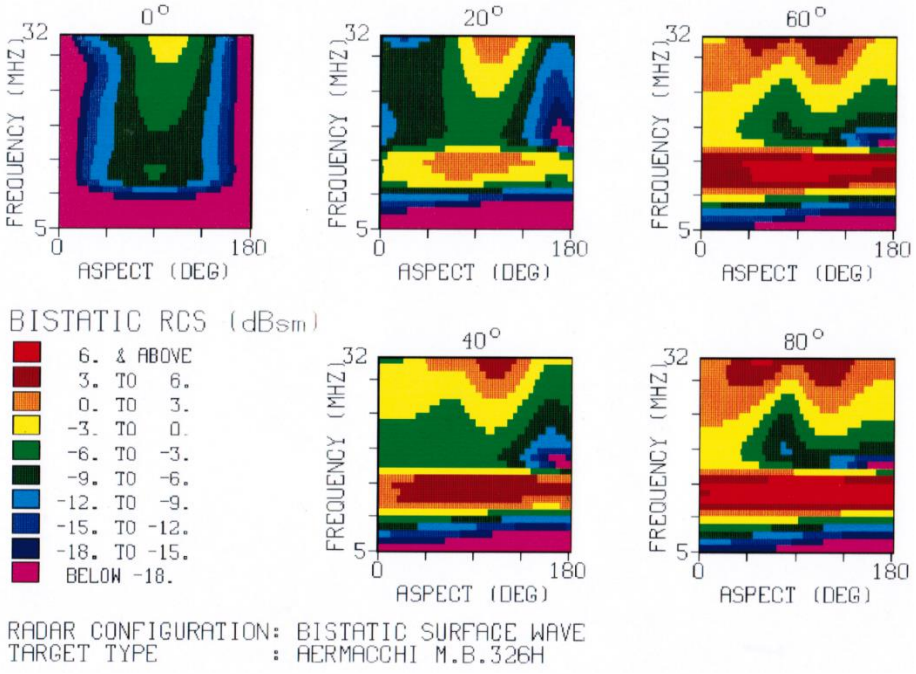

Figure 16. The HFSWR RCS of the Aermacchi MB 326H aircraft as a function of aspect and radar frequency. The five panels correspond to different bistatic angles as indicated.

3.4.3. Scattering from Slow-Moving Vehicles

Another example of the benefits of bistatic scattering at HF is the improved skywave detectability of slow land-based vehicles. Measurements of the spatial spectra of two types of terrain are presented in Figure 17a,b. These are based on very high-resolution digital elevation maps, covering thousands of square kilometers, with postings at 5 m spacing.

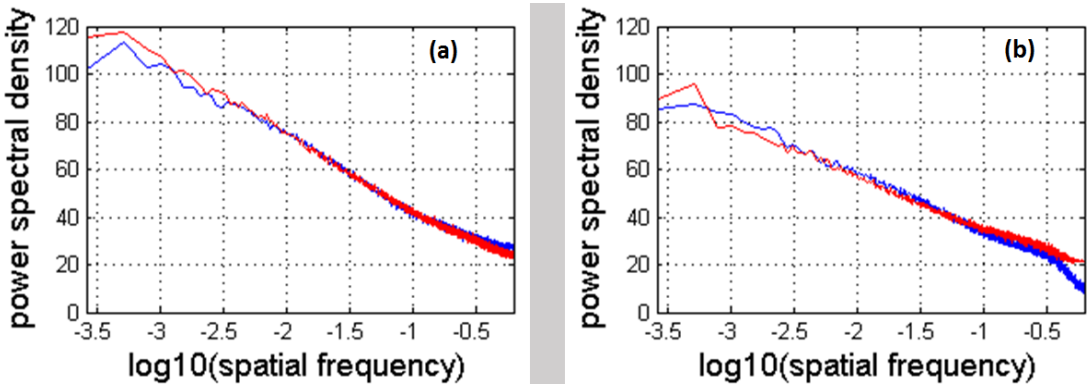

Figure 17. Power spectra of terrain elevation for (**a**) a hilly region, and (**b**) a relatively flat region.

From Figure 17a, corresponding to a hilly region, the surface elevation η follows a one-dimensional power law with $S(\kappa) \propto \kappa^{-3}$ while, for the relatively flat region treated in Figure 17b, the power law behaves as $S(\kappa) \propto \kappa^{-2.4}$. It is not unreasonable to regard these exponents as rough limits on typical terrestrial surfaces when the vegetation density is light. Now, the local HF bistatic scattering coefficient for natural land surfaces can be modelled with first-order small perturbation theory, taking account of the dependence of the scattering coefficient on the local angle of incidence, weighted by

the medium-scale slope probability density function. To proceed, we facet the resolution cell into n patches that are planar in the mean, but with small scale roughness,

$$\begin{array}{c}\sigma_{cell}(\theta_{scat},\varphi_{scat},\theta_{inc},\varphi_{inc}) = \int \sigma\left(\theta'_{scat},\varphi'_{scat},\theta'_{inc},\varphi'_{inc};\vec{r}\right)P\left(\theta'_{inc},\varphi'_{inc}\right)d\theta'_{inc}d\varphi'_{inc}d\vec{r} \\ = \sum_{m=1}^{n}\sigma\left(\theta'_{scat}(m),\varphi'_{scat}(m),\theta'_{inc}(m),\varphi'_{inc}(m)\right)\mu(\Delta_m)\end{array} \quad (13)$$

where the patches over each of which a local normal vector is defined are obtained by faceting the surface using a local flatness criterion.

The general expression for the first-order bistatic scattering coefficient takes the form

$$\begin{array}{c}\sigma^{(1)}_{pq}(\theta_{scat},\varphi_{scat},\theta_{inc},\varphi_{inc}) = 2^6\pi k_0^4 P_{pq}\sum_{m=1,2}S(k_0 sin\theta_{scat}cos(\varphi_{scat}-\varphi_{inc}) \\ -k_0 sin\ \theta_{inc},\ \ k_0\sin\theta_{scat}\ sin(\varphi_{scat}-\varphi_{inc}))\end{array} \quad (14)$$

where q and p index the incident and scattered polarisation states and the function P_{pq} accounts for the polarisation-dependence. To apply this to the tilted facets, we need only to transform to local coordinates via the appropriate rotation matrix, apply the scattering formula, then perform the inverse transformation.

There are two important considerations here that relate to the merits of bistatic scattering geometry. First, substituting the measured power laws of the land surfaces in the scattering formula, and writing the expression for the case of $\theta_{scat} = \theta_{inc} = \frac{\pi}{2}$ for clarity, we find

$$\sigma^{(1)}_{pq}\left(\frac{\pi}{2},\varphi_{scat},\frac{\pi}{2},\varphi_{inc}\right) \propto k_0^4.P_{pq}\left|k_0 cos(\varphi_{scat}-\varphi_{inc})-\ k_0\right|^{-\alpha} \equiv k_0^{4-\alpha}.\ P_{pq}\left|cos(\varphi_{scat}-\varphi_{inc})-1\right|^{-\alpha} \quad (15)$$

where $\alpha\ \epsilon[2.4,\ 3,]$. There are two features of interest here. The first is the slow fall-off of the power spectrum, which implies that the scattering coefficient will increase with radar frequency, so clutter can be reduced by operating at lower frequencies. The other feature is the variation of the scattering coefficient with bistatic angle. The case of the VV element of the polarization scattering matrix is plotted in Figure 18 over a typical range of bistatic angles. It is evident that by employing a moderately bistatic scattering geometry, the land clutter can be reduced by a factor of 2–3. As spectral leakage is a key limiting factor in slow land target detection, this is a significant gain in detectability.

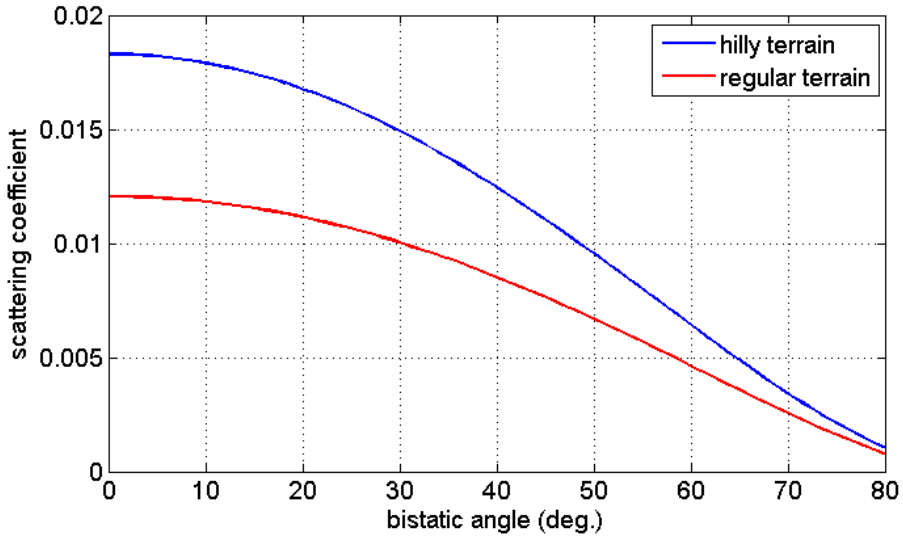

Figure 18. The variation of the VV scattering coefficient as a function of bistatic angle.

3.4.4. Scattering from Ship Wakes

The possibility of detecting ship wakes was recognized in the 1970s, but early studies focused on first-order scattering, which is critically dependent on radar geometry and frequency and hence

not a practical solution. The development of a second-order theory [38–40] has opened the way to a meaningful capability, but here too, careful consideration of the radar geometry and frequency is required to approach optimum sensitivity.

According to this theory, the wake signature depends not only on the vessel, it is also a function of the ambient sea state, so no simple assertion of optimality of one or other configuration can be made. Nevertheless, extensive modelling has shown that bistatic geometries routinely emerge as optimal solutions.

One indication of the possible advantage of bistatic geometry can be seen from Figure 19, showing a measured omni-directional wave spectrum from the open sea, on which is superimposed the corresponding spectrum for a ship wake. As the annotations reveal, the wake components are concentrated at low frequencies (and hence wavenumbers) for which monostatic first-order Bragg scatter at HF is not available, but at a bistatic angle φ the resonant wavenumber is decreased by a factor $\sin(\varphi/2)$.

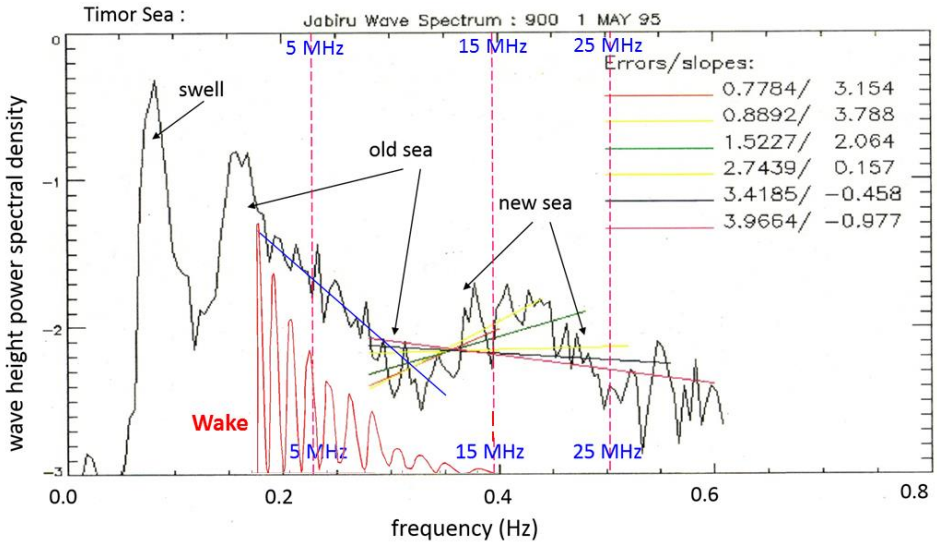

Figure 19. The omnidirectional spectrum of an ambient sea, and, superimposed (in red), the wake of a merchant ship at normal sailing speed; note that the abscissa is frequency, not wavenumber, connected here by the familiar deep-water dispersion relation. The radar frequencies corresponding to monostatic Bragg scatter are marked by the dashed lines.

3.4.5. Scattering from Ice-Covered Seas

There have been many oceanographic applications of HF radar but with a sole exception, they share the attribute that the dispersion relation assumed to govern the sea surface dynamics is that corresponding to a free water surface. In almost all applications, the general form of the dispersion relation,

$$\omega^2 = \left(g\kappa + \frac{\tau}{\rho}\kappa^3\right)\tanh\kappa H \tag{16}$$

is approximated by the inviscid, deep-water limit, $\tau \to 0$, $H \to \infty$

$$\omega^2 = g\kappa \tag{17}$$

though several studies have considered the shallow water case [29,41,42].

In the polar regions, the sea surface freezes and a complex ice structure forms over millions of square kilometers, varying dramatically with the season. This 'skin' is not completely rigid; it possesses mechanical properties that allow waves from the open sea to penetrate the ice zone, causing the surface to undulate as they propagate. In order to measure the surface motions and, from the Doppler

signature, infer the structural and mechanical properties of the ice, the free surface dispersion relation has to be replaced by a new model that takes flexural and viscoelastic characteristics into account. Moreover, the HF scattering theory that is the basis of radar echo interpretation has to be reformulated with the appropriate ice dispersion relation. Different forms of ice have different dispersion relations, so a prerequisite to ice field mapping is a computational scattering theory that can handle any situation. Such a theory has been developed and reported in [11,37]; it solves the forward problem for HF radar, treating the most general case of bistatic geometry and polarimetric dependence. Figure 20 compares the Doppler spectra for a particular sea state and radar configuration, with and without ice present.

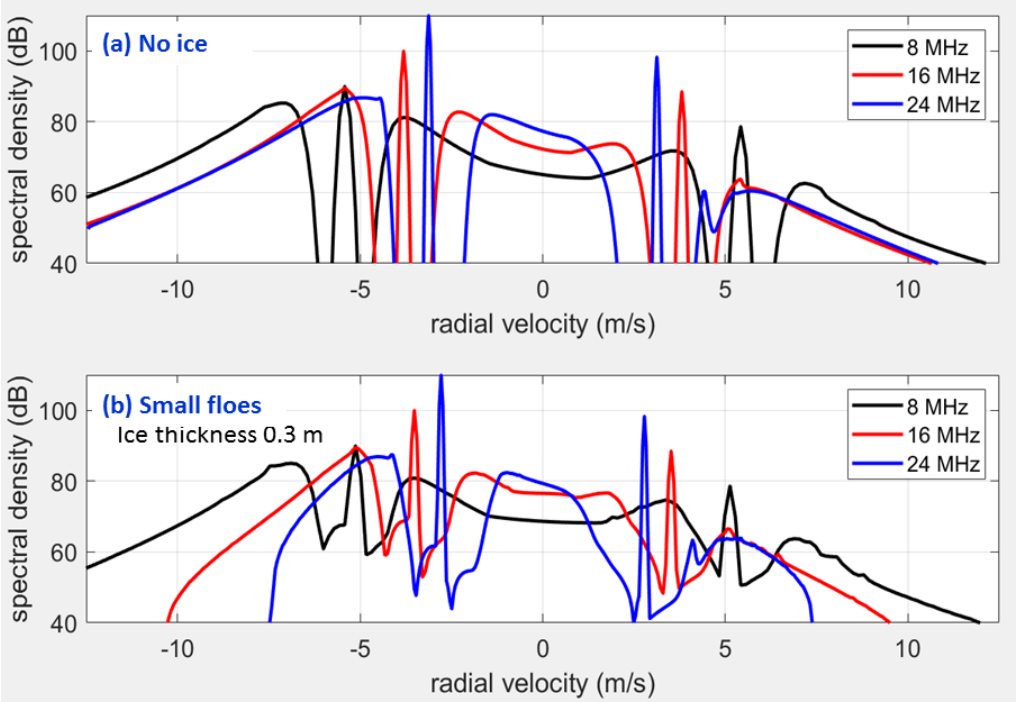

Figure 20. Doppler spectra computed for two situations: (**a**) A free ocean surface, and (**b**) a sea covered with small ice floes ('pancake' ice). Results for three radar frequencies are superimposed.

There are two key features of waves in the ice field that immediately draw our attention to bistatic HF radar geometries. First, the short waves tend to be attenuated far more quickly than long waves, in line with physical intuition. To give an idea of scale, waves in the swell frequency band can penetrate well over 100 km into the ice zone. Second, the most accessible properties of the ice that we seek to measure are encoded in the first-order Bragg scatter components. Together these imply is that we need to be able to sample the first-order Bragg scatter from the longer waves with our radars. As we noted earlier, bistatic scattering gives us greater access to the long waves.

Of course, the radar signal needs to propagate to areas of interest within the ice field, and this is another component of the remote sensing problem, but the local properties of the ice are reflected in the local ice dynamics and hence the local intrinsic Doppler spectrum.

3.4.6. Scattering from the Ionosphere

In addition to providing the propagation channel for HF skywave radar, the ionosphere is relevant to a wide range of human activities, so its physical properties are of keen interest. To HFSWR users, it poses a hazard in the form of field-aligned irregularities that result in ionospheric clutter, a potent source of obscuration of desired echoes. Techniques aimed at mitigating ionospheric clutter are employed in some systems but seldom achieve the goal of peeling away the elevated clutter to reveal the echoes from the sea. The most successful methods exploit detailed knowledge of the physics

involved, and this applies to other technologies that rely on the ionosphere, such as communication with spacecraft, and to climate studies.

To determine the properties of the ionosphere, various sounding systems are used. Vertical incidence sounders provide useful point information but to sample a wide area, we need to employ oblique illumination. Line-of-sight HF radars, included in the table of Figure 1, support some types of observation, but to obtain some more subtle properties, a bistatic sounding technique is required; that is, a form of bistatic radar. There is a vast literature on this, but for now it suffices to point out that the demands of modern HF radar systems go far beyond the 'traditional' channel transfer function parameterization—the distribution of energy over group range and Doppler [23]. More advanced applications of HF skywave radar and HF communications demand information on the structure and dynamics of the ionospheric plasma as manifested in wavefront geometry [14], repolarization and depolarization [15], wideband phase path modulation [13], nonlinear effects [25], and a variety of higher-order parameters. Bistatic skywave radar is a powerful tool for exploring these phenomena, as well as being a beneficiary of the derived knowledge.

3.4.7. Polarization Considerations in Bistatic Scattering Configurations

The scattering theories that are most widely employed to model HF radar scattering phenomena and hence to solve the associated inverse problems—the small perturbation method, the Born approximation, and physical optics—share the attribute that, at first order, they predict zero cross-polarized return for backscatter. If we wish to extract information from the cross-polarized components of the scattered field by applying the inverse scattering operator to the measurements, and staying with a monostatic radar configuration, we need to extend the theories to second order, thereby complicating the inversion procedures. Moreover, the cross-polarized elements of the monostatic polarization scattering matrix are frequently small, though this certainly may not be the case for the value of the information they contain. Not only can bistatic scattering geometries provide access to the cross-polarized echo information content at first order, it is often the case that cross-polarization becomes more significant as the bistatic angle increases. Thus, even at the quite fundamental level, there can be strong reasons for adopting a bistatic configuration even when a monostatic configuration is simpler to engineer and install.

That said, we need to bear in mind that the surface wave propagation mode heavily favours transverse magnetic field propagation (ie, approximately vertical, but with a forward tilt), the line-of-sight mode departs only slightly from being polarization-blind, and skywave propagation introduces complex field transformations, with both repolarization and depolarization [15] entering the picture. It follows that the practicalities of antenna design and installation are heavily dependent on the propagation modalities involved. Bistatic surface wave radars, like their monostatic counterparts, rely predominantly on relatively simple, vertically polarized antenna elements, though auxiliary horizontally polarized elements can be used to reduce external noise and interference very effectively. Purely line-of-sight radars in any configuration can measure the full scattering matrix, even through an intervening ionosphere [43], if they are equipped with appropriate dual-polarized elements. For skywave radars, it is not yet clear whether the cost and complexity of deploying a polarimetric capability can achieve, in practice, the benefits that theory suggests might be accessible. In particular, to design polarimetric antennas able to radiate a controlled polarization state over a substantial range of azimuths and elevations is a formidable challenge.

4. Bistatic Configurations that Are Currently of Particular Interest

The great majority of HF radar systems in operation today employ a single propagation mechanism, be it the skywave or surface wave mode. Recently, though, there has been a surge of interest in 'hybrid-mode' mode radars, so here we shall remark very briefly on three of these special configurations.

First consider these two configurations:

- The Tx→[skywave]→target→[surface-wave]→Rx configuration,

- The Tx→[skywave]→target→[line-of-sight]→Rx configuration.

These configurations are not new: Designs for both types were proposed in the 1980s for land-based transmitters and shore-based or shipborne receivers. Associated experiments carried out, but several studies concluded that these configurations were optimum only for niche applications. Nevertheless, the concept of augmenting skywave radars with forward-based receiving facilities was resurrected by several groups in the mid-2000s [44,45] and by others more recently [46–51]. To date, the modelling studies reported in the open literature have ignored many of the complexities of the skywave leg of the propagation path, though we may anticipate improvements in this area. The other area where endless complications enter the picture is platform dynamics and the associated impact on the Doppler spectrum of received signals, as noted in some recent publications [35,36,52–54].

We should also note the emergence of another, potentially potent configuration:

- Tx→[surface-wave]→target→[line-of-sight]→Rx, where the reception takes place in space.

Of the many non-standard configurations listed in Figure 1, this one has only recently been explored in the form where the receiver is mounted on an orbiting spacecraft; this is illustrated in the schematic in Figure 21a. As there are hundreds of HFSWR systems in operation, a single satellite might be able to collect information from a large number of radars as it travels around the Earth. Bernhardt et al. [55] conducted an experiment to test the closely related concept Tx→[skywave]→target→[line-of-sight]→Rx using the Canadian ePOP/CASSIOPE satellite and were able to identify land and sea features in the received echoes.

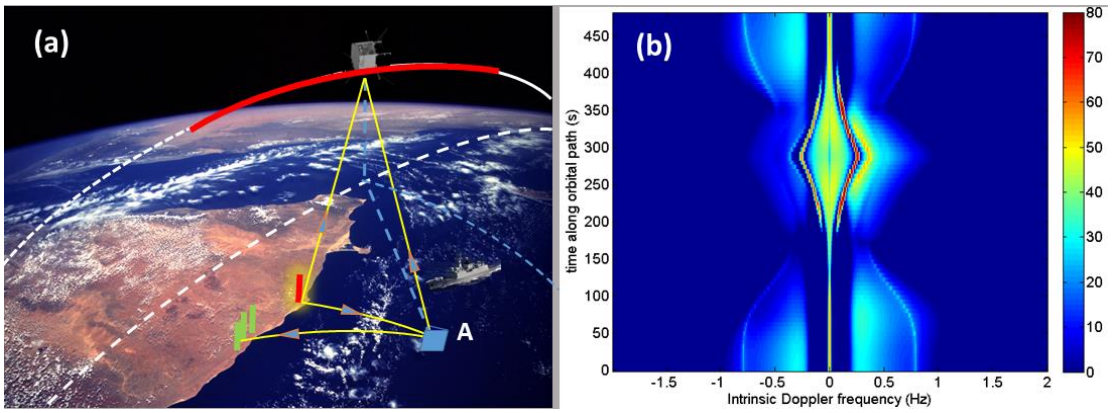

Figure 21. (**a**) The bistatic configuration of the satellite-borne receiver acquiring sea clutter echoes produced by a shore-based HFSWR, and (**b**) the computed Doppler spectrum of the signal arriving at points along the satellite orbital path.

An independent investigation [56] modelled the second-order intrinsic Doppler spectrum of the upwards-propagating signals as they reach orbital heights and demonstrated the viability of the concept by measuring the Doppler spectra of sea clutter collected over a Tx→[skywave]→target→[surface-wave]→Rx path. As shown in Figure 21b, the Doppler spectrum from a fixed patch on the sea varies in a complex and potentially highly informative way along the satellite's orbital path, though of course it must be acquired and processed by the spacecraft. Figure 22 depicts the geometry of an experiment that confirmed the viability of a signal path that includes mode (iii) as a subset in a time-reversed sense, i.e., retracing the signal path from receiver to sea to ionosphere.

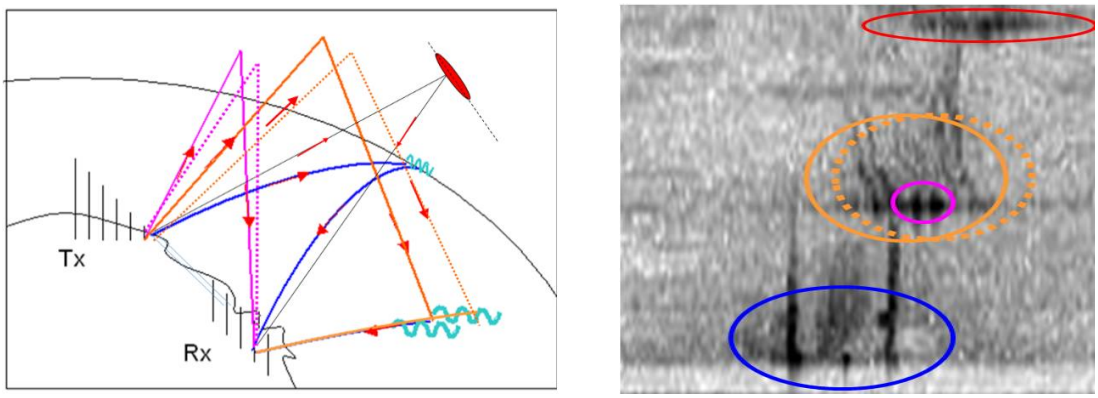

Figure 22. Experimental data from a nominal HF surface wave radar, which by happenstance recorded signals on Tx -> skywave -> sea scatter -> surface wave -> receiver. The magenta traces indicate the direct overhead reflection, the orange traces show the path of interest. Note that dual reflection points in the corrugated ionosphere provided a pair of echo traces in each case, slightly displaced in Doppler.

5. Site Selection for Bistatic HF Radars

If the challenge of optimum site selection for a monostatic radar may be considered difficult, then the equivalent task for a bistatic radar system is formidable. All the complexities of propagation and scattering that we have reviewed in the preceding pages must be taken into account and their impact assessed, carefully weighed against the missions to be addressed and the statistics of environmental parameters [57].

5.1. The Orthogonality Criterion

Intuitively, one might suspect that the benefits of bistatic configurations should be maximized when the bistatic angle is close to 90°, just as it is for stereoscopic radar configurations measuring currents or tracking targets—minimizing the well-known geometric dilution of precision (GDOP). This reasoning does not lead to practical or even good solutions for many applications. First, there is the obvious limitation of site availability—suitable locations offering near-orthogonality over the priority part of the coverage criterion may not be exist, or if they do, may be inaccessible for some reason. Second, near-orthogonality is no guarantee of increased radar cross section. Indeed, it is often the case that the bistatic RCS of targets of interest is consistently low for such scattering geometries; examining the trailing diagonal offset by 90° in either row or column space in Figure 9 makes this very clear.

Even for stereoscopic configurations, the issue of optimum radar disposition is nontrivial. As an example, in the case of ship detection against the sea clutter background, the signal-to-clutter ratio is not a monotonic function of bistatic angle, as shown schematically in Figure 23. While stereoscopic viewing clearly unmasks air targets, where the clutter may be taken as a narrow band centered on zero Doppler, the case for ship detection in clutter is complicated by the existence of Bragg line pairs and the associated second-order clutter. As shown in the figure, for some course-speed combinations, the ship can remain close to Bragg lines for both radars simultaneously.

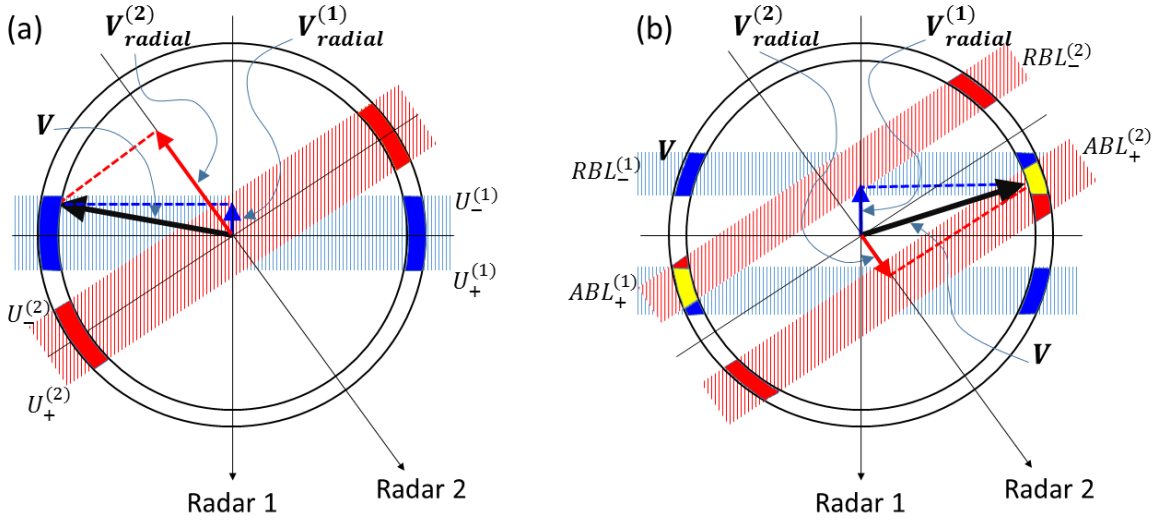

Figure 23. Blind speed diagrams for a bistatic radar system: (**a**) Aircraft detection, (**b**) ship detection. The blue arrows show the projection of the target velocity vector (black) onto the axis of Radar 1; the red arrows show the projection onto the axis of Radar 2. The blind speeds are shaded in the velocity annulus: Blue for Radar 1, red for Radar 2, yellow for doubly blind azimuths that can arise in the case of sea clutter.

Thus, an appreciation of the spatial distribution of the geometric attributes of a radar configuration plays a significant role in system design, and it has been found helpful to present this information in a graphical format. For the case of stereoscopic radar system operation, where the bistatic signal path may not be exploited, and focusing on current vector measurement and aircraft detection, where GDOP is important, it suffices to map the degree of orthogonality at each cell in the surveillance zone, as illustrated in Figure 24. It presents the information in two ways. Figure 24a plots the sine of the included angle in areas of common illumination, while Figure 24b converts this to yield the minimum radial speed that a target can present to one or other radar in its monostatic mode, expressed as a percentage of the target's actual speed. This kind of display facilitates site selection that optimizes performance over priority areas for the specified missions. It is a straightforward matter to generate equivalent displays for the case where bistatic modes of operation are available.

One must also bear in mind that potentially damaging crosstalk can occur when multiple radars in a network, perhaps stereoscopic, are obliged to share a common frequency band. In this circumstance, special signal processing is required to cancel the interfering transmissions [10].

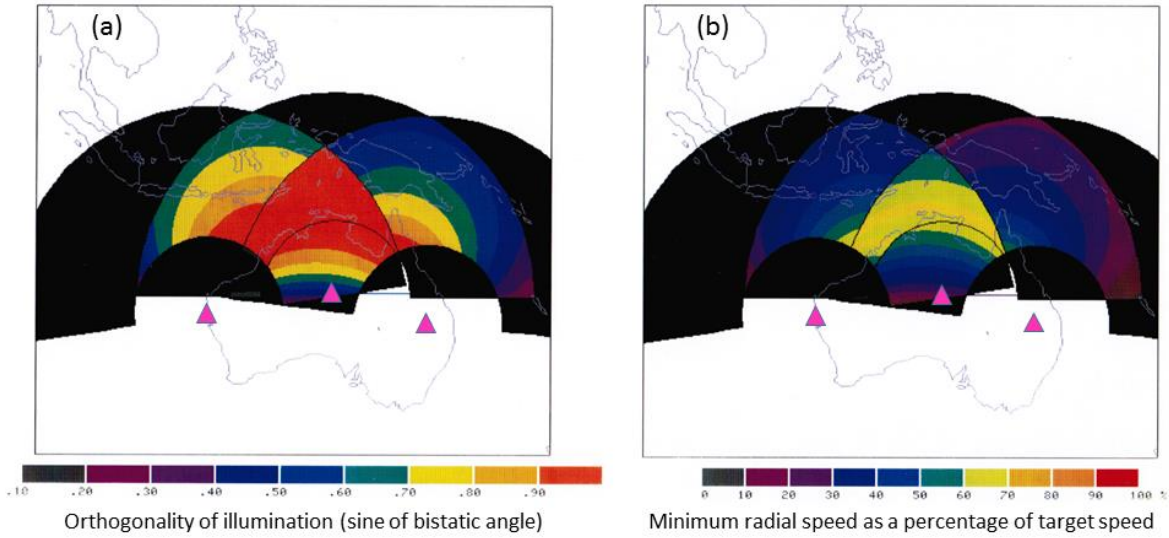

Figure 24. Trigonometric properties of overlapped radar coverage from the viewpoint of stereoscopic modes of operation. Figure 24a shows the degree of orthogonality as measured by the sine of the bistatic angle, while Figure 24b expresses it in terms of the minimum component of radial velocity that a target can present. The figure is for illustrative purposes only: The radar sites shown do not correspond to existing radars.

5.2. Site Selection via Multi-Objective Optimization

In order to take account of a multiplicity of mission types, each with its own performance criteria and dependence on prevailing environmental parameters, a far more rigorous approach to radar siting is needed. One methodology that has been used with success [58] is based on the concept of Pareto dominance. In this approach, a number of figures of merit are defined and then the site parameter space is searched to locate those solutions that possess the following property: That they are at least as good as their competitors against every FOM and better than any competitor in at least one FOM. The set of solutions that emerge from this search define the so-called Pareto front, and site selection can be carried out far more easily when one need only deal with this greatly reduced number of possibilities. Attributes such as clustering can be exploited to assess robustness of the solutions, and additional factors may then be taken into account, including less quantifiable criteria such as visual impact or even personal taste.

An important practical aspect of this methodology is its numerical implementation when the search space is large, as happens when one is designing a network of radars. Typically, one is confronted with need to select m sites out of n possibilities, where m is modest, but n may be large. One study of the South China Sea [59] encountered a sample space of ~10^{23} solutions. To handle realistic cases successfully, an efficient nonlinear optimization algorithm is essential. One such technique has been reported in [60]; it employs a genetic algorithm fitted with a special acceleration routine that enables it to address highly demanding radar network design problems.

6. Conclusions

It may seem surprising that we have not partitioned this paper into distinct sections dealing with individual radar configurations, such as skywave and surface wave radars. Our decision was based on two considerations. First, bistatic configurations such as the hybrid sky–surface mode obviously straddle the disciplines that may be relevant to either skywave or surface wave monostatic radars, but not both. Second, and just as importantly, during half a century of first-hand experience with several forms of HF radar, we frequently encountered circumstances where cross-fertilization of ideas provided significant benefits.

Accordingly, in this paper, we have set out with four goals:

(i) To present a taxonomy that encompasses essentially all possible HF radar configurations;
(ii) To illustrate how bistatic geometries impact on the various components of the radar process;
(iii) To provide some examples of missions for which bistatic geometries offer distinct advantages;
(iv) To describe some practical techniques that have been found efficacious in the design and siting of bistatic HF radar systems

The taxonomy speaks for itself; it may serve to provoke thought on the possible merits of alternative bistatic configurations in particular applications. The consequences of bistatism for waveforms, propagation, scattering, and so on extend beyond the brief treatment we have provided here, but hopefully the underlying message is clear: Some of the basic radar principles that we take for granted and seldom bother to reflect upon need careful re-examination when we leave the monostatic domain. We have described several radar missions where clear benefits of bistatic configurations are evident; some of these missions are familiar ones that have long been addressed with monostatic configurations, but others, such as ice monitoring and characterization, ship wake detection and analysis, and space-borne interception of HFSWR clutter for global scale radio oceanography are only now entering the HF radar user's lexicon. The list is hardly exhaustive, and no doubt there are surprises in store for us all. Finally, the practical techniques that are mentioned in the text have all been used successfully in serious applications.

Funding: This research received no external funding.

Conflicts of Interest: The author declares no conflict of interest.

References

1. Headrick, J.M.; Anderson, S.J. HF Over-the-Horizon Radar, Chapter 20. In *Radar Handbook*, 3rd ed.; Skolnik, M., Ed.; McGraw-Hill: New York, NY, USA, 2008.
2. Roarty, H.; Cook, T.; Hazard, L.; Harlan, J.; Cosoli, S.; Wyatt, L.; Alvarez Fanjul, E.; Terrill, E.; Otero, M.; Largier, J.; et al. The global high frequency radar network. *Front. Mar. Sci.* **2019**. [CrossRef]
3. Lyon, E. Missile Attack Warning. In *Advances in Bistatic Radar*; Willis, N.J., Griffiths, H.D., Eds.; SCITECH Publishing: Rayleight, NC, USA, 2007; pp. 47–55.
4. CODAR Ocean Sensors. Available online: http://www.codar.com/SeaSonde.shtml (accessed on 17 January 2020).
5. WERA Ocean Radar. Available online: https://helzel-messtechnik.de/de/6035-WERA-Remote-Ocean-Sensing (accessed on 17 January 2020).
6. Cosoli, S.; de Vos, S. Interoperability of direction-finding and beam-forming high-frequency radar systems: An example from the Australian high-frequency ocean radar network. *Remote Sens.* **2019**, *11*, 291. [CrossRef]
7. Australian Defence Business Review. June 2019. Available online: https://adbr.com.au/over-the-horizon/ (accessed on 17 January 2020).
8. Raytheon Relocatable Over-the-Horizon Radar (ROTHR) for Homeland Security. Available online: http://www.mobileradar.org/Documents/ROTHR.pdf (accessed on 17 January 2020).
9. Francis, D.B.; Cervera, M.A.; Frazer, G.J. Performance prediction for design of a network of skywave over-the-horizon radars. *IEEE Aerosp. Electron. Syst. Mag.* **2017**, *32*, 18–28. [CrossRef]
10. Zhang, Y.; Frazer, G.J.; Amin, M.G. Simultaneous operation of two over-the-horizon radars. In Proceedings of the SPIE 5559, Advanced Signal Processing Algorithms, Architectures and Implementations XIV, Denver, CO, USA, 26 October 2004.
11. Anderson, S.J. Monitoring the marginal ice zone with HF radar. In Proceedings of the IEEE Radar Conference, Seattle, WA, USA, 8–12 May 2017.
12. Parent, J.; Bourdillon, A. A method to correct HF skywave backscattered signals for ionospheric frequency modulation. *IEEE Trans. Antennas Propag.* **1988**, *36*, 127–135. [CrossRef]
13. Anderson, S.J.; Abramovich, Y.I. A unified approach to detection, classification and correction of ionospheric distortion in HF skywave radar systems. *Radio Sci.* **1998**, *33*, 1055–1067. [CrossRef]
14. Anderson, S.J. Multiple scattering of HF skywave radar signals—Physics, interpretation and exploitation. In Proceedings of the IEEE Radar Conference, Rome, Italy, 26–30 May 2008.

15. Anderson, S.J. Skywave channel characterisation for polarimetric OTH radar. In Proceedings of the IEEE US Radar Conference, Philadelphia, PA, USA, 2–6 May 2016.
16. Anderson, S.J. The Challenge of Signal Processing for HF Over-the-Horizon Radar. In Proceedings of the Workshop on Signal Processing and Applications (WOSPA'93), Queensland University of Technology, Brisbane, Australia, 13–15 December 1993.
17. Anderson, S.J. OTH Radar Phenomenology: Signal Interpretation and Target Characterization at HF. *IEEE Aerosp. Electron. Syst. Mag.* **2017**, *32*, 4–16. [CrossRef]
18. Anderson, S.J. Limitations to the extraction of information from multihop skywave radar signals. In Proceedings of the IEEE International Conference on Radar, Adelaide, Australia, 3–5 September 2003.
19. Purdy, D.S. Receiver antenna scan rate requirements needed to implement pulse chasing in a bistatic radar receiver. *IEEE Trans. Aerosp. Electron. Syst.* **2001**, *37*, 285–288. [CrossRef]
20. Willis, N. *Bistatic Radar*; SCITECH Publishing: Rayleigh, NC, USA, 2005.
21. Anderson, S.J. Multiple scattering of HF surface waves: Implications for radar design and sea clutter interpretation. *IET Radar Sonar Navig.* **2010**, *4*, 195–208. [CrossRef]
22. Anderson, S.J. Scattering effects on DOA estimation and geolocation from HF surface wave intercepts. In Proceedings of the HF/DF Symposium, South-West Research Institute, San Antonio, TX, USA, 10–12 May 2008.
23. Earl, G.F.; Ward, B.D. The frequency management system of the Jindalee over-the-horizon backscatter HF radar. *Radio Sci.* **1987**, *22*, 275–291. [CrossRef]
24. Anderson, S.J. Stereoscopic and Bistatic Skywave Radars: Assessment of Capabilities and Limitations. In Proceedings of the Radarcon-90, Adelaide, Australia, 18–20 April 1990; pp. 305–313.
25. Anderson, S.J. Nonlinear scattering at HF: Prospects for exploitation in OTH radar systems. *Turk. J. Electron. Eng. Comput. Sci.* **2010**, *18*, 439–456.
26. Barrick, D.E. Remote Sensing of sea state by radar. In *Remote Sensing of the Troposphere*; Derr, V.E., Ed.; NOAA/Environmental Research Laboratories: Boulder, CO, USA, 1972; Chapter 12.
27. Rice, S.O. Reflection of EM waves from slightly rough surfaces. Comm. *Pure Appl. Math.* **1951**, *4*, 351–378. [CrossRef]
28. Johnstone, D. *Second-Order Electromagnetic and Hydrodynamic Effects in High-Frequency Radio Wave Scattering from the Sea*; Technical Report 3615-3; Stanford Electronics Laboratories, Stanford University: Stanford, CA, USA, 1975.
29. Barrick, D.E.; Lipa, B.J. The second-order shallow water hydrodynamic coupling coefficient in interpretation of HF radar sea echo. *IEEE J. Ocean. Eng.* **1986**, *11*, 310–315. [CrossRef]
30. Anderson, S.J.; Anderson, W.C. Bistatic scattering from the ocean surface and its application to remote sensing of seastate. In Proceedings of the IEEE APS International Symposium, Blacksburg, VA, USA, 15–19 June 1987.
31. Srivastava, S.K.; Walsh, J. An analysis of the second-order Doppler return from the ocean surface. *IEEE J. Oceanic Eng.* **1985**, *10*, 443–445. [CrossRef]
32. Walsh, J. *On the Theory of Electromagnetic Propagation across a Rough Surface and Calculations in the VHF Region*; Technical Report N00232; DREA: Ottawa, ON, Canada, 1980.
33. Gill, E.W.; Walsh, J. High-frequency bistatic cross sections of the ocean surface. *Radio Sci.* **2002**, *36*, 1459–1475. [CrossRef]
34. Gill, E.W.; Huang, W.; Walsh, J. On the development of a second-order bistatic radar cross section of the ocean surface: A high frequency results for a finite scattering patch. *IEEE J. Oceanic Eng.* **2004**, *31*, 740–750. [CrossRef]
35. Walsh, J.; Huang, W.; Gill, E.W. The first-order high frequency radar ocean surface cross section for an antenna on a floating platform. *IEEE Trans. Antennas Propag.* **2010**, *58*, 2994–3003. [CrossRef]
36. Walsh, J.; Huang, W.; Gill, E.W. The second-order high frequency radar ocean surface cross section for an antenna on a floating platform. *IEEE Trans. Antennas Propag.* **2012**, *60*, 4804–4813. [CrossRef]
37. Anderson, S.J. Prospects for the inversion of HF radar echoes from sea ice to recover structural and viscoelastic parameters. In Proceedings of the 3rd Australasian Conference on Wave Science, Auckland, New Zealand, 12–14 February 2018.
38. Anderson, S.J. HF radar signatures of ship and submarine wakes. *J. Eng.* **2019**, *2019*, 7512–7520. [CrossRef]
39. Anderson, S.J. Sensitivity of HF radar signatures of ship wakes to hull geometry parameters. In Proceedings of the 21st Australasian Fluid Mechanics Conference, Adelaide, Australia, 10–13 December 2018.

40. Anderson, S.J. An OTH Plimsoll line? Remote measurement of ship loading with HF Radar. In Proceedings of the IEEE International Conference Radar 2019, Toulon, France, 23–27 September 2019.
41. Holden, G.J.; Wyatt, L.R. Extraction of sea state in shallow water using HF radar. *IET Proc. F (Radar Signal Process.)* **1992**, *139*, 175–181. [CrossRef]
42. Lipa, B.; Nyden, B.; Barrick, D.E.; Kohut, J. HF radar sea-echo from shallow water. *Sensors* **2008**, *8*, 4611–4635. [CrossRef]
43. Anderson, S.J.; Abramovich, Y.I.; Boerner, W.-M. On the solvability of some inverse problems in radar polarimetry. In Proceedings of the SPIE Conference on Wideband Interferometric Sensing and Imaging Polarimetry, San Diego, CA, USA, 23 December 1997; Volume 3120.
44. Frazer, G.J. Forward based receiver augmentation for OTHR. In Proceedings of the IEEE Radar Conference, Boston, MA, USA, 17–20 May 2007; pp. 373–378.
45. Riddolls, R. *Ship Detection Performance of a High Frequency Hybrid Sky-Surface Wave Radar*; Ottawa Technical Memorandum TM 2007-327; Defence R&D Canada: Ottawa, ON, Canada, 2007.
46. Li, Y.J.; Wei, Y.S.; Xu, R.Q.; Shang, C. Simulation analysis and experimentation study on sea clutter spectrum for high-frequency hybrid sky-surface wave propagation mode. *IET Radar Sonar Navig.* **2014**, *8*, 917–930.
47. Zhu, Y.P.; Wei, Y.S.; Li, Y.J. First order sea clutter model for HF hybrid sky-surface wave radar. *Radioengineering* **2014**, *23*, 1180–1191.
48. Walsh, J.; Gill, E.W.; Huang, W.M.; Chen, S. On the development of a high-frequency radar cross section model for mixed path ionosphere–ocean propagation. *IEEE Trans. Antennas Prop.* **2015**, *63*, 2655–2664. [CrossRef]
49. Chen, S.; Gill, E.W.; Huang, W.M. A first-order HF radar cross-section model for mixed-path ionosphere–ocean propagation with an FMCW source. *IEEE J. Ocean Eng.* **2016**, *41*, 982–992. [CrossRef]
50. Wang, S.W.; Li, Y.J.; Xu, R.Q.; Wei, Y.S.; Wang, Z.Q.; Sheng, S. Research on characteristics of first-order sea clutter for HF sky-surface wave radar. *IET Microw. Antennas Propag.* **2016**, *10*, 1124–1134.
51. Yang, L.W.; Fan, J.M.; Guo, L.X.; Liu, W.; Li, X.; Feng, J.; Lou, P.; Lu, Z.X. Simulation analysis and experimental study on the echo characteristics of high-frequency hybrid sky–surface wave propagation mode. *IEEE Trans. Antennas Propag.* **2018**, *66*, 4821–4831. [CrossRef]
52. Ma, Y.; Gill, E.W.; Huang, W.M. First-order bistatic high-frequency radar ocean surface cross-section for an antenna on a floating platform. *IET Radar Sonar Navig.* **2016**, *10*, 1136–1144. [CrossRef]
53. Ma, Y.; Huang, W.M.; Gill, E.W. The Second-Order Bistatic High-Frequency Radar Cross Section of Ocean Surface for an Antenna on a Floating Platform. *Can. J. Remote Sens.* **2016**, *42*. [CrossRef]
54. Ma, Y.; Huang, W.M.; Gill, E.W. Bistatic high-frequency radar ocean surface cross section for an FMCW source with an antenna on a floating platform. *Int. J. Antennas Propag.* **2016**. [CrossRef]
55. Bernhardt, P.A.; Siefring, C.L.; Briczinski, S.C.; Vierinen, J.; Miller, E.; Howarth, A.; James, H.G.; Blincoe, E. Bistatic observations of the ocean surface with HF radar, satellite and airborne receivers. In Proceedings of the IEEE OCEANS 2017-Anchorage, Anchorage, AK, USA, 18–21 September 2017; pp. 1–5.
56. Anderson, S.J. Space-borne interception of HF radar echoes for environmental intelligence. In Proceedings of the 16th Australian Space Research Conference, Melbourne, Australia, 26–28 September 2016.
57. Anderson, S.J. Optimising bistatic HF radar configurations for target and environmental signature discrimination. In Proceedings of the IEEE Conference on Information, Decision and Control, Adelaide, Australia, 12–14 February 2007.
58. Anderson, S.J. Optimizing HF radar siting for surveillance and remote sensing in the Strait of Malacca. *IEEE Trans. Geosci. Remote Sens.* **2013**, *51*, 1805–1816. [CrossRef]
59. Anderson, S.J. HF radar network design for remote sensing of the South China Sea. In *Geoscience and Remote Sensing*; Margheny, M., Ed.; InTech: London, UK, 2014.
60. Anderson, S.J.; Darces, M.; Helier, M.; Payet, N. Accelerated convergence of genetic algorithms for application to real-time problems. In Proceedings of the 4th International Symposium on Inverse Problems, Design and Optimization, Albi, France, 26–28 June 2013.